Quantifying the Adhesion Strength of Microalgae on Polydimethylsiloxane Surfaces

by

Zhijing (Celebi) Wan
B.Sc., University of British Columbia, 2018

A Thesis Submitted in Partial Fulfillment of the
Requirements for the Degree of

MASTER OF SCIENCE

in the Department of Chemistry

Quantifying the Adhesion Strength of Microalgae on Polydimethylsiloxane Surfaces

by

Zhijing Wan
B.Sc., University of British Columbia, 2018

Supervisory committee

Dr. Dennis K. Hore, Supervisor
(Department of Chemistry)

Dr. Diana E. Varela, Departmental Member
(Department of Biology)

ABSTRACT

Silicone rubber is a promising candidate for the next generation of electrical insulators on account of the prolonged hydrophobicity of the polymers. However, microalgae biofouling is always a concern for high voltage insulators installed in coastal regions. To understand how microalgae species interact with polymer surfaces that are used in electrical insulator applications, a study has been conducted to determine the interactions of a benthic and a pelagic algal species with polydimethylsiloxane surfaces. The adhesion strength of algal species were quantified with two different types of flow cells employed for our studies. These two types of flow cells are microfluidic chips and a laser-cut flow cell chamber, which provide a high and low wall shear stress, respectively. A video analysis software was designed to automate all aspects of the flow rate profile, data acquisition, and image analysis. Pristine poly(dimethyl siloxane) (PDMS), deionized water-exposed PDMS, and salt solution-exposed PDMS samples were used as substrates in adhesion experiments. The results indicate that surface hydrophobicity played a critical role in adhesion strength. At low shear stress, both *B. braunii* and *T. rotula* cells demonstrate a strongest adhesion strength onto the pristine PDMS surface, while show the weakest adhesion strength onto the salt solution exposed PDMS surface. At high shear stress, all PDMS surfaces provide an equal adhesion environment to the both species.

Contents

List of Figures

List of Symbols and Definitions

symbol	definition
AFM	atomic force microscop
ATR	attenuated total reflection
DC	direct current
DI	deionized
EPS	extracellular polymeric substances
FTIR	Fourier-transform infrared spectroscopy
HVI	high voltage insulator
PDMS	polydimethylsiloxane
SIR	silicone rubber
(X)DLVO	(extended) Derjaguin, Landau, Verwey, Overbeek approach
B. braunii	*Botryococcus braunii*
T. rotula	*Thalassiosira rotula*
a	radius of the arbitrary object, m
c	maximum particle dimension, m
D	diameter of the capsule shaped object, m
d	diameter of the capsule shaped object, m
H	distance between the surface and centre of the equivalent sphere, m
h	the half depth of the channel, m
k	wall correction coefficient
L	characterized length, m
l	the shortest distance from the center of the particles to the wall, m
Q	volumetric flow rate, $\mathrm{m}^3 \cdot s^{-1}$
R	radius of the spherical or cylindrical object, m
S	shear rate of the flow, m

U	flow velocity, m·s^{-1}
w	the width of the channel, m
Re	Reynolds number
$\dot{\gamma}$	wall shear rate, s^{-1}
μ	dynamic viscosity of water at 20 °C, 8.9×10^{-4} Pa·s
ρ	density of water at 20 °C, 997 kg·m^{-3}
F_d	drag force, N
$F_{d\infty}$	drag force on the particle when moving in the unbounded medium, N

ACKNOWLEDGEMENTS

My thesis would not be finished without the help, advice and support from numerous individuals. I would like to express my sincere gratitude to these people here.

I would first like to thank my supervisor, Dr. Dennis Hore. He consistently allowed this thesis to be my own work but steered me in the right the direction whenever he thought I needed it. Without his passionate help and input, the study could not have been conducted successfully.

I would also like to thank Dr. Diana Varela and Dr. Katherine Elvira as well as members of their research groups, for their great insight and technical help with micro-algal culture and microfluidics, respectively.

Thank you to my fellow lab members for being a supportive group.

Special thanks to my parents for supporting me, financially and mentally. I would like to acknowledge Waltfred Lee for his assistance in fluid mechanics study, his love and patient. This thesis is dedicated to the memory of my great grandmom, who passed away in May 2019.

Chapter 1

Introduction

1.1 Biofouling

It costs billions of dollars a year to control and remove the accumulation of unwanted material in industrial equipment. Industrial fouling consists with two different types. Inorganic fouling composes of deposits from corrosion, crystallization, suspended particles, oil and ice. On the other hand, biofouling refers to micro or macro biological organisms accumulation. Biofouling leads to health risks in the medical field and financial loss in the industrial and marine field. For instance, bacteria can colonize on medical devices such as implants, biosensors, catheters, which posing a huge risk to patients [1]. In the marine system, it had been reported that the US Navy cost 1 billion every year to deal with biofouling problems [2].

In the marine industry, ships, sonar devices, pontoons, offshore structures, intake pipes, power plants, underwater instruments and seawater cooling systems are all impacted by marine biofouling. Ships performance is severely influenced by fouler. The study found that even increasing the biological slime thickness for 1 mm, there was an 80% increase in skin friction and a 15% loss in ship speed compared with values obtained for a clean hull [3]. Furthermore, biofouling on the inner wall of pipelines can decrease the heat exchange efficiency or even clog the pipeline for water transfer [4]. Biofouling on ship hulls is also a transfer vector for coastal invasions [5]. Chan *et al.* found that even though survival rates of biofoulers on military ships during round-trip voyages was relative low,

there was still a possibility to introduce non indigenous species from temperate to Arctic ports in Canada [6].

Microalgae plays a key role in the marine system, they are the major biofoulers to all surfaces exposed to an aqueous environment. However, the adhesion mechanisms between microalgae to surfaces are inconclusive and the process of biofilm formation is still unclear. In this section, three types of microalgae, cyanobacteria, diatom and green algae are introduced with their cell physiologies and some current studies about their biofilm formation.

1.1.1 Cyanobacteria

There are a large amount of research in bacterial adhesion on surfaces including silicone rubber [7], stainless steel [8] or nanostructural films [9]. Cyanobacteria, so called blue green algae, are one of the common species to form biofilms on different kinds of surfaces. Cyanobacteria are unicellular organisms that do not have nuclear membranes, while have photosynthetic pigments in the peripheral region of the protoplast [10]. Cyanobacteria were commonly found living in freshwater, soil or other environments with pH range around 7–8 for most species [10], however, the extreme limit of pH is ranging from 5–10. Cyanobacteria that can tolerate high concentrations of salt solution, but they prefer to live in alkaline solution [10]. On the other hand, cyanobacteria were well known to adapt to extremes of temperature [10]. They are a predominant species found in hot springs, with temperature higher than 40 ^{o}C [10]. One study had shown that a cyanobacterium, *Chroococcidiopsis fissurarum* had different growth trends on rough fired brick surfaces regardless of the environmental temperature. The same study demonstrated that when relative humidity was smaller than 98%, no growth accrued. Hence, a highly humid environment was crucial to cyanobacteria survival [11]. Cyanobacteria need essential mineral nutrients to conduct nitrogen fixation, making themselves good providers of nitrogen fertilizer [10]. They are also good photosynthesizers who contain chlorophyll

a, phycocyanin and allophycocyanin as pigments for photosynthesis [10].

With these outstanding features, cyanobacteria can adapt to various environments with low nutrient requirements and easily form biofilm on almost any surfaces. Similar to other microorganisms, the key element to establish bioflims is extracellular polymeric substances (EPS) [12]. The components for these secretions are heteropolysaccharides, DNA, peptides and fats for cyanobacteria [12]. Fucose, rhamnose, arabinose, galactose, glucose, mannose, xylose, galacturonic acid and glucuronic acid are the common monosaccharides constitute in cyanobacterial EPS and galactose is the most frequent monosaccharides that found out in cyanobacterial EPS [12]. Moreover, if cyanobacterial cells experience a lack of nutrients, EPS synthesis can be stimulated and enhanced [12]. Mucilaginous layers of EPS surrounds to single cell or cell aggregates, so called by sheath [12], such sheath play a role in adhesive interaction between cell to cell and cell to surface. The secretion of some monosaccharides such as fucose and rhamnose leads EPS to be more hydrophobic, enhancing adhesion performance [12]. The accumulation of EPS on solid-liquid interface causes changes to physio-chemical properties of surfaces like free surface energy, hydrophobicity or surface charge density [13].

On the other hand, although cyanobacteria produce large amounts of EPS, they were also well known as good producers of bioactive substances with potential antifouling properties [14]. Fish and Codd found that one cyanobacterium, *Phormidium sp.* had an anti-microbial compounds that can be produced to against a wide range of other microorganism [14]. Antibiotic compounds such as lipophilic malyngamide, neurotoxin and cyanobacterin that can be isolated from cyanobacteria showed a strong ability to prevent fouling by bacteria and macro-organisms [14].

1.1.2 Diatom

Microalgae also include diatoms (bacillariophceae), a group of unicellular protists. They live in both aquatic (both salt and fresh water systems) and terrestrial habitats. They

have a siliceous cell wall (two valves and girdle bands) [15]. Diatoms play an important role in the global silica cycle. Diatoms utilize silicic acid in the ocean to construct their cell walls, which influences their primary productivity [16]. Diatoms have plasmid membranes with four layers of chloroplast envelope, a chloroplast endoplasmic reticulum membrane, mitochondrial membrane, nuclear membrane and thylakoid membrane. [17] Unlike cyanobacteria which only contain chlorophyll *a* as pigment, diatoms contain both chlorophyll *a* and chlorophyll *c*. The predominant light-harvesting pigment chlorophyll *a* collects energy from the sun and turns it into chemical energy through photosynthesis. While chlorophyll *c* is an antenna pigment, producing an additional strong blue absorption band [18]. N, P, Si and Fe are key elements for diatom growth and uptake. Diatoms would become dominant species in the phytoplankton community when such aquatic environments are satisfied with high concentration of elements above. However, diatoms reduce their size when they experience a depletion of nutrients [19].Moreover, studies have been found that diatoms are major contributors to primary production in the world's oceans. However, diatom adhesion and bioflim formation are less studied.

Like cyanobacteria, EPS produced by diatoms, are also called mucilage, that mainly consist of polysaccharides and they are useful for attachment of the diatoms to the solid substratum. The morphology of these EPS are diversified, forms ranging from adhering films/capsules, tubes, pads, stalks and cell coating. [20] EPS secretion is involved in the motility mechanism of diatoms [21]. There were hypotheses stated that EPS secreted from raphe, labiate process and deep groove located between two valves were responsible for motility to different diatom species. [21] On the other hand, Gordon *et al.* stated that force of EPS hydration outside raphe should be the one responsible for diatom motility [21]. EPS produced by diatoms also associate with more permanent adhesion to substratum. Studies demonstrated that stalk-form mucilage contained sulfated polysaccharides, which made EPS structure more flexible. Such flexible EPS communities provided adaptive advantages for those diatoms attached to surfaces experiencing water current [21].

Benthic diatoms are major foulers of artificial surfaces in the marine environment, functionality of artificial surfaces are severely affected. Good examples of surface efficiency and costs of biofouling is ocean going vessels [22]. Large increase in fuel costs through increased weight and hydrodynamic drag due to the heavy slime layers dominated by diatoms [22]. Increased emissions, marine shipping fleets use engines that are already one of the worst polluting sources per ton of fuel [22]. Typical genera commonly documented to be problematic biofoulers inculde: *Amphora*, *Craspedostauros*, *Toxarium*, *Licmophora*, *Navicula*, *Nitzschia*, *Cocconeis* and *Achnanthes*. [22] Kiørboe *et al.* quantified stickiness of diatom cells to produce aggregates upon collision with other cells. They found that *T. pseudonana* stickiness increased with increasing C:N ratio (nutrient limitation) and cell division ceased. Also, nutrient limitation most likely to occur is after a phytoplankton bloom based on new nutrients which depletes at a rate faster than remineralization can occur.

1.1.3 Green Algae

Green algae is a large and diversified group consisting of *Chlorophyta* and *Charophyta*, both of phylums contain macro and micro-algae [23]. Such microalgae have cell size around 5–15 μm with simple morphology like sarcinoid cell packages, or branched filaments [24]. Unlike cyanobacteria and diatom, study of biofilm formation of green microalgae are less developed. Researchers in German studied calcifying biofilms in two exemplar karst-water creeks, which were dominated by diatoms and cyanobacteria producing significant amounts of EPS [25]. Interestingly, researchers unexpectedly found that green micro-algae were also in this community. However, scientists cannot ensure the appearance of green microalgae was due to the preference in calcifying biofilm or by accidents [26]. Same study had been also found out that compare to the red algae and the diatom, two green algae (*Chlorella vulgaris* and *Chlorella autotrophica*) produced constant amount of EPS while others produced larger amount of EPS over time.

1.2 Silicone Rubber Insulators and PDMS

1.2.1 Silicone Rubber Insulators

An electrical insulator in a high voltage system (HVI) is designed to support a charged conductor and provide an isolating path. Large amounts of HVI are used in overhead power lines to transmit power and distribute networks. The materials of those HVI need their charges are not free to move through their body, consisting of a very low conductivity. The traditional HVI are made by ceramic and glass over the past 120 years, such materials have good resistance against environmental aging [27]. However, because of the surface hydrophilicity of these materials, they have poor resistance in enviromental pollution [27]. Compared to ceramic and glass insulators, polymer insulators that appeared in the 1960s showed great advantages in their better hydrophobicity, lower leakage current, resistance to vandalism and higher mechanical strength [27].

Silicone rubber (SIR) is the dominant product in polymer insulators. Silicone rubber is a high molecular weight linear polymer, with chains consisting of silicon and oxygen atoms. The generic formula of silicone is R_2SiO, where R can be an organic functional groups such as methyl or phenyl or vinyl or trifluoropropyl [28]. The attachment of organic function groups to an inorganic backbone can delocalize σ electrons along to silicone backbone [28]. One unique property of silicone rubbers is that they are very flexible. The Si–O–Si bond angle is can ranging from 140°–180° [29]. Silicone rubber has a higher oxygen permeability under room temperature, which is 21 times higher compared to natural rubber [29]. On the other hand, Si–C bond is much stronger than C–C bond, leading these polymers to have a better heat resistance, electric conductivity and chemical stability [28]. Silicone rubber can be used for long term at 150 °C and short term at 200–300 °C and Embrittlement point is -70 to -60 °C [28]. This thermal resistance is due to high dissociate energy of the Si–C bond [28]. Silicone rubber has high insulation resistance of 1-–100 TΩ and particularly has a outstanding performance in resistance of corona discharge, making

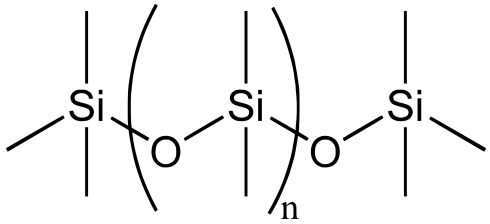

Figure 1.1: Chemical structure of silicone.

it a good candidate for HVI [28]. Silicone rubber also does not swell organic oil and has a high degree of chemical inertness [28].

1.2.2 Surface Modification under Electrical Stress

SIR HVI are used for high direct current (DC) voltage long distance transmission lines. However, high DC voltage stress leads to problems. Gustavsson *et al.* demonstrated that DC stress caused higher degree of surface erosion and higher leakage current [30]. Bruce *et al.* used a DC inclined plane test to investigate further that compared to negative DC voltage, positive DC voltage is more damaging to SIR surface [31]. While other study had been found the DC negative impulse voltage would become more negative due to the pre-deposited negative charges on SIR surface [32]. One major failure of SIR HVI is the higher leakage currents and flashover accidents due to the DC power transmission. The unidirectional electrostatic field brings contamination (sea coast, salt soils) from surrounding onto HVI, leading to surface degradation and then leakage flow. Moist contaminates become conductive and induces currents in the pollution layer, leading to leakage current. The flow of leakage current heats up the insulator surface, causing some parts of the insulator dry out. This mechanism is called dry band arcing [33]. Arshad *et al.* showed that the breakdown strength of insulators was reduced due to higher level of pollution and leads to flashover at lower electric field [33]; results of FTIR showed that amount of O-H radicals increased in SIR after flashover occurred while Si–CH_3, Si$(CH_3)_2$, Si–O–Si and CH groups decreased [33].

Electric fields can be intensified at the sharp corners, projecting points, edges of metal

surfaces or small diameter wires due to the humid atmosphere around SIR HVI. This leads to a transient gaseous ionization in an insulation system when the voltage stresses or voltage gradient exceeds its critical value and the mechanism called corona discharge. Corona discharge is another common aging mechanism to SIR HVI due to high electrical stress from HVDC energized power lines. It had been found that cloth wiping, a maintenance work to SIR HVI, caused corona discharging by triboelectric effect and 80% surface charges need 4 more hours to decay [32]. Zhu *et al.* demonstrated that exposure to corona discharge led to SIR surface surface degradation and hydrophobicity loss; results of FTIR showed OH stretch simultaneously appeared after the corona discharge treatment [34]. Reddy *et al.* observed intense surface oxidation and hydroxylation due to acid fog on the corona performance of the SIR surface, bringing down long term performance of HVI [35].

1.2.3 Surface Modification under Environmental Stress

If insulators are installed surround by ocean, sea water spray spreads with the wind, forming salt layers on insulator surfaces. Hence, salt contamination is considered as one major aging factor under environmental stress. Study has found that polydimethylsiloxane (PDMS) is semi-permeable to fine salt powders. When PDMS-salt mixtures immersed in water, water can enter into mixed compounds and dissolve salt grains in the mix compound, forming pockets. Due to osmotic differential pressure, those pockets lead to internal cracks in the SIR and eventually, the portion of salt solution in those pockets flows out to the external water environment through the cracks [36]. The same study found that insulator end-fittings and connections heavily corroded due to salt contamination since those are the parts where rain cannot reach, and the same study found leakage current levels were high during the periods of salt fog spraying [37]. Kim *et al.* showed that contact angle of room temperature vulcanizing silicone rubber reduced as a function of time in the salt fog chamber. FTIR results from the same study demonstrated that there was a reorientation of hydrophobic methyl-groups on SIR surface [38]. Allen *et al.* showed that weight, firmness and surface

smoothness were reduced when SIR fully immersed in 3% salt solution at 80 °C [39]. The later study from the same group using molecular dynamics simulation proved that chlorine ions appear to have much higher diffusivities into SIR compared to sodium ions and water molecules. Therefore, depolymerization via hydrolysis is might due to the high diffusivities of chlorine ions. Moreover, hypochlorous acid might be produced when SIR experienced low voltage stress and salt contamination on the surfaces [40].

On the other hand, UV radiation is another factor causing outdoor SIR HVI degradation. The frequency, of tensile strength and elongation at the break can be found in UV aged SIR sample [41]. It has been found out that the Si=C bond has weak resistance to UVC, which has wavelength between 100–290 nm. Under UV rays, the predominant reaction is cross-linking, which involves the methyl group in PDMS [42]. Hydrophobicity of SIR surface is lost under high intensity of UV lamp with wavelength range between 250 to 350 nm [42]. However, the effect of UV radiation to SIR surface hydrophobicity is controversial. Some studies have shown that UV radiation only slightly decreases SIR surface hydrophobicity [43]. Other research even found out that hydrophobicity can be improved for some aged SIR samples [44].

1.2.4 Surface Modification under Biological Stress

Microorganism biofilm adhered on silicone rubber SIR HVI causing several severe problems such as fouling, degradation,discolouration, penetration and odor [45]. The surface hydrophobicity can be reduced by covering by hydrophilic biofilm. In one of the study, researchers collected biofilm samples on SIR HVI in three different locations: Tanzania, Sri Lanka and Sweden. Results showed that the dominant species (unicellular green algae associated with bacteria and filamentous fungi) and mechanism of biofilm formation were similar among the samples from three different continents [46]. Green algae contamination was severe to a 500 kV high voltage transmission in Guangdong, China due to its humid environment. Most of biofilm was found on the sheds and sheaths

Figure 1.2: Illustration of the microalgae biofilm on the electrical insulator [7].

from the middle parts of the insulators. Silicone content of the insulator where covered by green algal biofilm was significantly lower [47]. Yang *et al.* determined that the hydrophobicity was lost when SIR was covered by green algae and humidity was the main reason to influence the change of surface hydrophobicity. The same study also stated that flashover voltage decreased in the place where the surface was covered by higher density of cells [7, 48]. The distribution of biofilm is varied on an insulator. The horizontal part of the insulator (shed) tends to have a higher microbial growth than the vertical part of the insulator (shank). This is due to the water accumulation on the horizontal part of the insulator. Ouyang *et al.* found that the optimal growth condition for algal community living on SIR was a temperature in the range of 15–25 °C, a light intensity in the range of 1000–4000 lx, and a humidity level higher than 70% [48]. Same study also revealed that the aging of the SIR surfaces due to algal biofouling was minor [48].

1.3 System to Test Cell Adhesion Strength

Characterizing the ability of cells to adhere onto artificial substrates has broad applications in a variety of technology and industrial areas. For example, bacterial adhesion to ship hulls is responsible for the subsequent adhesion of larger marine species such as barnacles that creates additional drag for ships, resulting in a large excess of fuel required [49]. In many industrial processes, heat exchangers are used for heating or cooling process liquids. Adhesion of cells to the metal surfaces reduces the heat transfer, and therefore either greatly increases costs associated with heating, or can create dangerous situations where streams are not sufficiently cooled [50]. In biomedical applications there are situations where material surfaces are tailored to either promote or inhibit the adhesion of specific cells [49]. For example, adsorption of proteins blocks the activity of biosensors [51]. In the repair of spinal cord injuries, it is important that neurons can grow on engineered scaffolds inserted into the gaps [52].

1.3.1 General Methods for Characterization Cell Adhesion

There are many techniques that can provide information on cell adhesion. These range from simple observation-based methods where the number of adhered cells are counted and tabulated per unit area, to methods that can provide quantitative descriptions of the adhesion forces. One of the way was measuring adhesiveness and stiffness by using a micro needle to pull apart an attached pair of cells. The adhesiveness was measured by bending produced in a micro needle [53]. Some examples of these methods are mechanical contact techniques including atomic force microscopy and related methods [54, 55]. It has been investigated the cell to surface adhesion force between *Enterococcus faecalis* to polymers using atomic force microscopy (AFM) and EPS was observed on polymer adhered bacterial cells. Later on, atomic force microscopy are more often used in cell to cell adhesion study. The interaction between melanoma cells and endothelial cell layers was quantified using AFM. This system was established that has a vertical range of movement of 100 μm, which

increased in pulling distance sufficient for the observation of long-distance interactions without reducing the imaging capabilities of the AFM [56]. Mulansky*et al.* developed a novel protocol to characterize the early stages of bacterial biofilm formation using AFM. *E. coli* were attached to polyethyleneimine coated beats and these beads were glued to the cantilever. Practically, this protocol alleviated the complexity of AFM operations and offered a result in more reliable production of usable cell probes [54]. Another method that is similar to AFM is micro cantilever deflection-based methods [55]. A micro cantilever setup was developed to measure directly the shear strength based on the force-displacement curve to detach a cell from a surface in a cell [55]. One of the study described attaching yeast cells to fluorescent microspheres using flow cytometers. The percentage of cells with microspheres attached and cell population distribution pattern were obtained. This method provided a quantitative, automated and fast way to analyze cell-substratum interaction [57]. The other common way to test cell-substratum adhesion was the centrifugation assay, that set of sealed microtiter plate wells were coated by target cells and cells were separated from substratum by centrifuge force [58].

1.3.2 Quantifying Cell Adhesion using Flow Chamber

Other techniques evaluate the adhesion strength by the application of shear using a flow chamber. This method was inspired by vascular endothelial cells experiencing shearing stresses generated by blood flow. Parallel plate flow chambers became popular to test cell-substratum adhesion in the 1990s. This kind of flow chamber generates constant stress gradient over the entire length of the chamber and setup theory is based on Hele-Shaw flow [59]. Lawrence *et al.* used a parallel plate chamber with a well-defined flow field to test adhesion of polymorphonuclear leukocytes (PMNL) to human umbilical vein endothelial cells (HUVEC). The flow chamber was set up with one side of a HUVEC monolayer and the other side was polycarbonate. These two sides were secured by rubber gaskets with an internal gap around 250 μm. Inverted-stage microscope, syringe pump and digital camera

were attached to the chamber as well. PMNL suspension was then perfused through the flow chamber and the number of attached PMNL were counted after 10 min [60]. Most flow cell chambers can only observe cell adhesion from the top view, Cao *et al.* developed a flow chamber set up that can observe the side of the cell under dynamic flow conditions. The side view flow chamber can observe cell-surface interaction and cell perpendicular motion more directly. Instead of placing the inverted microscope to the bottom of chamber, Cao *et al.* used two optical prisms with a 45° chromium-coated surface to change light pathway and observed side view of the chamber [61]. One advantage of flow-based systems is that they are capable of providing low shear to study weakly-adherent cells, with adhesion forces less than 1 nN, while contact-probe methods have a lower limit of 1–100 nM. This is especially interesting for studies of cells such as algae that do not adhere strongly [61].

This current study was inspired from the adhesion study of algal cells to surfaces by Ozkan and Berberoglu [62, 63]. In these papers, researchers developed a simple flow chamber to test planktonic and benthic algal cells adhesion strength to hydrophobic and hydrophilic substrata. The parallel plate flow cell chamber was assembled with the test materials as substrates, one PDMS spacer with 0.075 cm thick and one polycarbonate sheet as top layer. The PDMS spacer was designed with certain dimensions to ensure a smooth and laminar flow in the flow cell, the culture medium was introduced at the inlet and slowly expanded at an angle of 15°. During the adhesion experiment, the syringe pump delivered the cell suspension from the reservoir to the flow chamber with the pre-determined flow rates. Study also adopted thermodynamic approaches (Derjaguin, Landau, Verwey, Overbeek (DLVO) approach and Extended Derjaguin, Landau, Verwey, Overbeek (XDLVO) approach) to model surface interactions and compared with experimental results. The results showed that XDLVO theory is the great model to predict cell adhesion to different types of surfaces. Researchers then adopted XDLVO theory to various types of microalgal cells and test cell to cell and cell to surface interactions. The conclusion was that hydrophilic algae to hydrophilic coatings over surfaces is the ideal condition to minimize

microalgal biofouling.

1.3.3 Fluid Mechanics

The Navier-Stokes equations are partial differential equations describing the motion of an incompressible fluid,

$$\frac{\partial \rho}{\partial t} + \overrightarrow{\nabla} \cdot (\rho \overrightarrow{u}) = 0 \tag{1.1}$$

$$\frac{\partial (\rho \overrightarrow{u})}{\partial t} + \overrightarrow{\nabla} \cdot [\rho \overline{\overline{u \otimes u}}] = -\overrightarrow{\nabla} p + \mu \overrightarrow{\nabla}^2 \cdot u + F \tag{1.2}$$

where ρ is the density of the fluid, u is the velocity field of a fluid, μ is the dynamic viscosity of the fluid, p is the fluid pressure field and F captures the effects of external forces. Equation 1.1 described conservation of mass, or called continuity equations. Equation 1.2 is Newton's second law, or the conservation of momentum in terms of internal and external force. Here $\otimes$ denotes the tensorial product, forming a tensor from the constituent vectors. A double bar denotes a tensor. The Reynolds number, *Re*, a dimensionless parameter defined as the ratio of inertial and viscous forces in a fluid,

$$Re = \frac{\rho U L}{\mu} \tag{1.3}$$

where U is flow velocity; L is the characterized length, which can be chosen in many different ways. One common L is the diameter of spherical objects in the flow. Reynolds number can be defined as the hydraulic diameter of the channel as well. For a fully developed laminar flow with very low flow rate between two parallel plates, where the fluid is extremely viscous and fluid inertia is negligible compared with viscous forces. This type of flow is Stokes flow or creeping flow regime, usually with Reynolds number $Re \ll 1$, leading to the non-dimensionalization of the equation 1.2, which becomes

$$-\overrightarrow{\nabla} p + \mu \overrightarrow{\nabla}^2 \cdot U = 0. \tag{1.4}$$

Equations 1.1 and 1.4 should be applied in flow with wall-bounded (certainly applies when viscous forces are dominant) or select the boundary at infinity [64].

Spherical objects. Stokes law describes the drag force exerted on spherical objects with very small Reynolds numbers in Stokes flow regime. The drag force is expressed as

$$F_{\text{drag}} = 6\pi\mu RU \tag{1.5}$$

where R is the radius of the spherical object. With assumptions that flow is laminar, surface is smooth and spherical particles do not interfere with each other. However, if flow is in wall-bounded, Stokes formula has to be adjusted for the influence from the wall by a Goldman wall correction function f that depends on the object-to-wall distance [65],

$$F_{\text{drag}} = f\left(\frac{H}{R_e}\right) 6\pi\mu R_e U \tag{1.6}$$

where R_e is the equivalent radius of the sphere and H is the distance between the surface and centre of the equivalent sphere. The analytical solution for the Goldman wall correction function is 1.7009. Reynolds number Re used hydraulic diameter of the channel as characterised length,

$$Re = \frac{2\rho Q}{(w+2h)\mu} \tag{1.7}$$

where w is width of channel and h is half depth of the channel. The velocity field of a fluid, U, is a parabolic flow profile obeys Poiseuille law, defined as

$$U(H) = 6\frac{Q}{hw}\frac{H}{h}\left(1-\frac{H}{h}\right) \tag{1.8}$$

where Q is the volumetric flow rate. The detailed fluid profile is shown in Figure 1.3.

Capsule-shaped objects. Most cases only studied spherical objects to obtain drag force since spherical symmetry (symmetry around a point) numerically is easier to solve than other azimuthal symmetry (symmetry along an axis). There are some studies about azimuthal symmetry or arbitrary objects in Stokes flow. Wiklund *et al.* proposed an analytical drag force interpolation formula that is based on the full solution of the Navier–Stokes equations for capsule-shaped objects. The drag force is modified as:

$$F_{\text{drag}} = f_i(\frac{H}{R_e}, E) 6\pi\mu R_e U \tag{1.9}$$

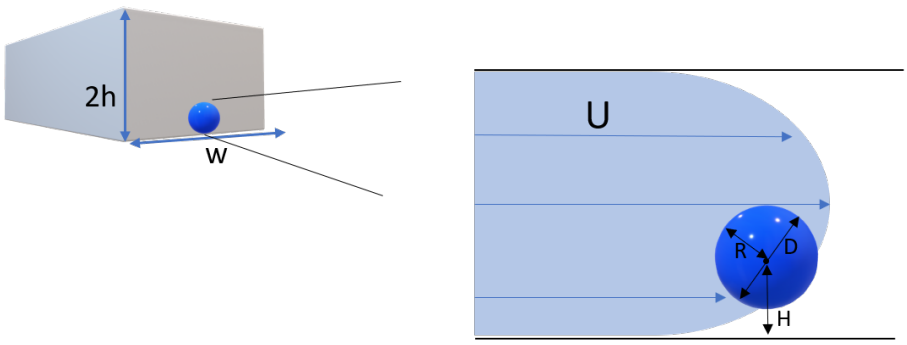

Figure 1.3: Illustration of the spherical object exposed to a fluid flow in a rectangular channel.

$$U = SH \tag{1.10}$$

$$E = \frac{L}{D} \tag{1.11}$$

where S is the shear rate of the flow; E is aspect ratio and D is the diameter of the capsule shaped object and ratio range is 1 to 5. Reynolds number modified as,

$$Re = \frac{\rho SHD}{\mu} \tag{1.12}$$

The Goldman correction factor f_i modified as:

$$f_i(\frac{H}{R_e}, E) = a_i(E)(\frac{H}{R})^{-c_i(E)} + b_i(E) \tag{1.13}$$

For parallel case, the coefficient functions are:

$$\begin{aligned} a_{\parallel} &= 0.700 + 0.448(E-1)^{1.007} \\ b_{\parallel} &= 1.001 + 0.320(E-1)^{0.863} \\ c_{\parallel} &= 1.082 + 0.032(E-1)^{0.414} \end{aligned} \tag{1.14}$$

For perpendicular case, the coefficient functions are:

$$\begin{aligned} a_{\perp} &= 0.700 + 0.902(E-1)^{1.046} \\ b_{\perp} &= 1.001 + 0.463(E-1)^{0.862} \\ a_{\perp} &= 1.082 + 0.046(E-1)^{0.831} \end{aligned} \tag{1.15}$$

The detailed fluid profile shows in figure 1.4.

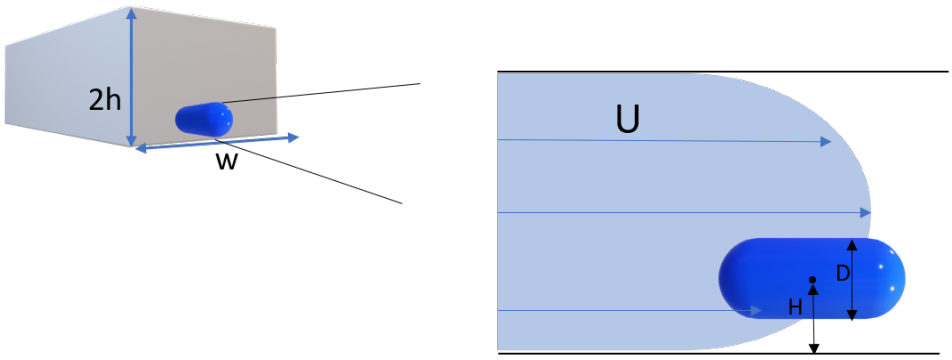

Figure 1.4: Illustration of the capsule-shaped object exposed to a fluid flow in a rectangular channel.

Table 1.1: Drag force of different shapes of particle in the infinite domain [67]

Particle shape	drag force (infinite domain)
Hemispherical cup	$17.525\mu aU$
Flat disk of radius a	$16\mu aU$ (broadside) and $32/3\pi\mu aU$ (edge-on)
Sphere of radius a	$6\pi\mu aU$
Prolate spheriod	$8\pi\alpha\mu aU$
Oblate spheriod	$8\pi\beta\mu aU$

Arbitrary-shaped objects. On the other hand, Brenner studied the effect of finite boundaries on the Stokes resistance of an arbitrary particles [66]. For the correction function to the Stokes law resistance is then of the form:

$$K_d = \frac{F_d}{F_{d\infty}} = \frac{1}{1 - k(F_{d\infty}/6\pi\mu Ul) + O(c/l)^3} \tag{1.16}$$

where F_d is the drag force on the particle when moving in the bounded medium while $F_{d\infty}$ is the drag force on the particle when moving in the unbounded medium; c is the maximum particle dimension and l is the shortest distance from the center of the particles to the wall;k is a coefficient that depends the nature of boundary but not nature of particle; $O(c/l)^3$ gives the drag on the sphere to the third order of approximation.

However, back to 1851 when Stokes investigated fluid flow in a very slow motion, he found out in two dimensional scale, there can be no Stokes flow of a fluid around a flat disk, or is no non-trivial steady-state solution for the Stokes equations around an infinitely long cylinder in three dimensional scale. The fact is opposite with his own findings of

Table 1.2: Wall correction coefficient for typical boundaries [66]

Boundary	Location of the particle	Direction of motion	k
Circular Cylinder	Axis	Axial	2.10444
Parallel plane walls	Middle plane	Parallel to walls	1.004
Single plane walls		Parallel to wall	9/16
Spherical	Center		9/4

the stationary sphere in Stokes flow. This flaw was caused by large distance separation of the bounded walls. With the boundary separation infinitely large, the Reynolds number cannot be small in the outer flow region, leading to a non-uniform approximation to the total velocity distribution.

In 1910, Oseen proposed that inertia terms should be retained in the far field, where the fluid velocity is approximately equal to flow velocity. He suggested modifying the inertial terms in the Navier-Stokes equations, which become dominant far from the cylinder. Based on Oseen's approximation, Lamb in 1911 then provided another simpler approximation of the flow around the cylinder and an analytical expression for drag coefficient [68],

$$\frac{F_d(k=0,Re)}{\mu U_0} = \frac{4\pi}{1/2-\gamma-ln(Re/4)} \tag{1.17}$$

$$Re = \frac{\rho U R}{\mu} \tag{1.18}$$

where k=R/h is object with radius R in mid way between two two parallel plane walls h (Figure 1.5), k=0 means object is in infinite domain, $\gamma = 0.57721$ is Euler's constant.

In a semi-infinite viscous liquid bounded by a single plane wall, Takaisi in 1955 got analytical drag force on circular cylinder of infinite length parallel to its bounding single wall [68],

$$\frac{F_d(e)}{\mu U_0} = \frac{4\pi}{ln(2e)} \tag{1.19}$$

where e=$d/R \geq 2$, d is the distance between the cylinder axis and the single wall.

For the same condition above, Jefferey and Onishi gave the exact solution to calculate drag force for $1 \leq e < \infty$ [68],

$$\frac{F_d(e)}{\mu U_0} = \frac{4\pi}{ln(e+\sqrt{e^2-1})} \tag{1.20}$$

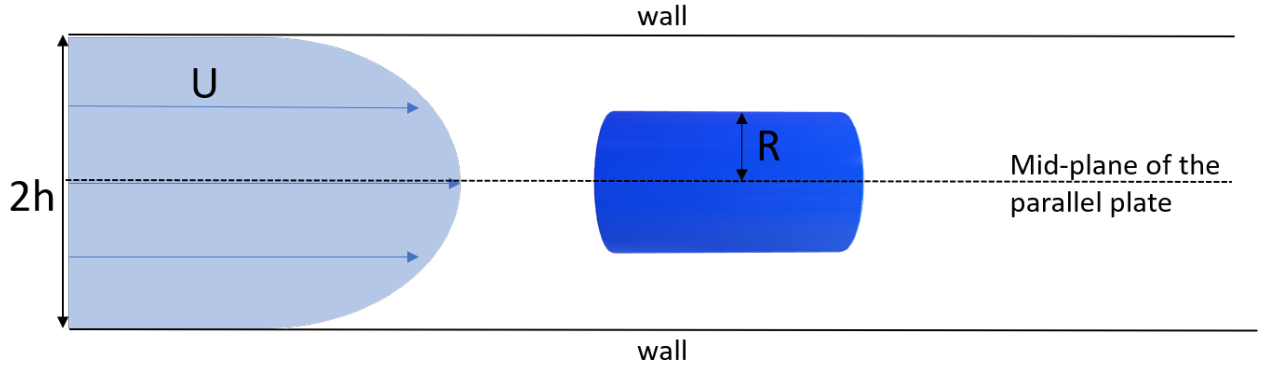

Figure 1.5: Illustration of the cylindrical object exposed to a fluid flow in a rectangular channel.

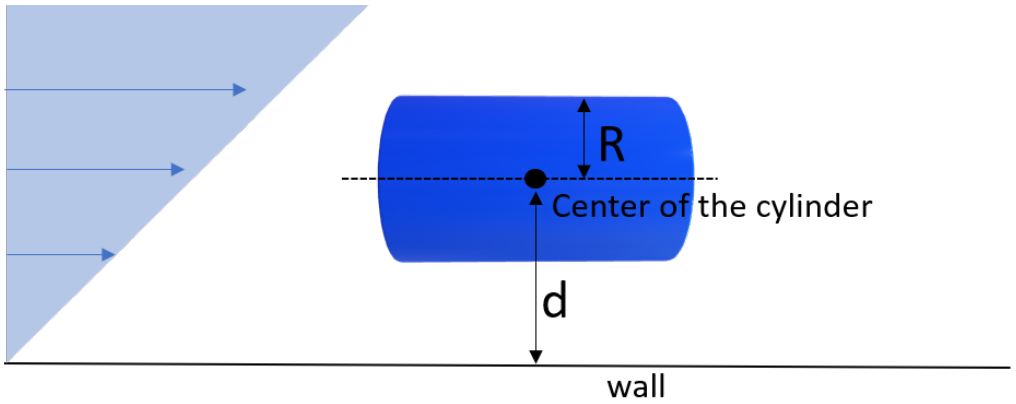

Figure 1.6: Illustration of the cylindrical object exposed to a fluid flow in a rectangular channel.

and when the cylinder is moving in very close to the single wall ($e \approx 1$),

$$\frac{F_d(e)}{\mu U_0} = 2\pi\sqrt{2}(e-1)^{1/2} \tag{1.21}$$

In conclusion, this section describes how the shear rate to be converted to drag force, which is the major force acts on the spherical shaped. capsule shaped and arbitrary shaped cells, for adhesion experiments.

1.4 Objectives

Although previous studies have investigated mechanisms of bacterial or fungal adhesion onto diversified surfaces, quantifying micro algal adhesion forces onto polymer surfaces

are lacking. This thesis seeks to directly investigate two micro-algal cells adhering onto PDMS surfaces. More specifically, there are two main objectives.

1. Investigating the physio-chemical surface properties of polymer and the interaction between micro algal cells with polymer surfaces.

2. Quantifying micro algal adhesion forces onto polymer surfaces with different treatment conditions.

Due to the large difference in adhesion force between our target cells (benthic *B. braunii* and pelagic *T. rotula*), two different types of flow cells were employed for our studies. Low shear rates for weakly-adhered cell were achieved using a flow cell with an 800 μm channel depth. To achieve high shear rates, microfluidic chips were used for strong-adhered cell. Knowing the dimensions of the channel, the shear can be calculated from the volumetric flow rate. Finally, fluid mechanics can be used to estimate the adhesion force from the cell morphology.

Chapter 2

Quantifying the Adhesion of Green Algae onto Polydimethylsiloxane Surface

2.1 Introduction

Botryococcus braunii (*B. braunii*) is one of the benthic species, who featured with massive production of hydrocarbon oil as well as polysaccharides and carotenoids, which can transform to biodiesel [69] [70]. The size of *B. braunii* colony is generally ranging from 30 μm to 2 mm, compared to an individual cell which is 7 μm to 13 μm [71]. The aggregates are immersed in an oily extracellular matrix [69]. Thus, *B. braunii* is an excellent candidate for biofilm formation.

Microfluidics is a flow cell technique with channel height in micrometers. Such technologies can integrate numerous biological and chemical analyses into understanding the proprieties and evolution of biofilms. These microsystems can precisely control cell culture and zoom into single-cell resolution to observe the cell behaviors. One study has demonstrated a high-throughput photobioreactor array that can manipulate single-colony resolution for photosynthetic microorganisms under 64 different light conditions. By using this platform, *B. braunii* cells were characterized in their growth and oil production.

There are some previous studies that testing adhesion strength between benthic green cells and substrates by using microfluidic devices. This chapter investigates the adhesion strength between *B. braunii* and PDMS surfaces by using microfluidic chips. The adhesion

force was measured for surfaces that (i) without any stress (pristine), (ii) under pure water exposure, and (iii) under salt solution exposure. PDMS microfluidic chips are used in the following cell adhesion strength test because they are structurally similar to a silicone rubber-based electrical insulator and also able to handle high shear stress flows.

2.2 Materials and Methods

2.2.1 Algal Culturing and Sample Preparation

Botryococcus braunii (*B. braunii*) (UTEX 572) were obtained from the Culture Collection of Algae at the University of Texas at Austin, UTEX. The algae were cultivated as batch cultures in BG-11 nutrient medium [72] under 12:12 light: dark cycle with irradiation of 15.6 ± 2.2 μE·m^{-2}·s^{-1} and steady temperature 20 °C. The pH of the medium was adjusted by 1 M NaOH and 1 M of HCl to 7.6 ± 0.1. Subculture was done every 5 to 6 weeks by inoculating 2 mL of cell culture to 250 mL new medium. Cells in their log phase, around 6–8 d were collected to obtain morphology tests and adhesion strength experiments [73]. 1 mL of cell culture was collected in the log phase and was sonicated for 30 s with one second on and one second off mode. Then culture was centrifuged at 3000 rpm for 5 min, washed twice and re-suspended in phosphate-buffered saline (PBS) containing 1.62 mM KH_2PO_4, 6.49 mM K_2HPO_4, and 1.35 mM NaCl. Eventually, the culture was re-suspended in 1 mL BG-11 medium and be prepared to be injected into microfluidic chips.

2.2.2 Characterization of Morphological Properties of Algal Cells

Morphological properties of cells were quantified based on their images obtained with a lab-built inverted microscope [74], Image J Software was used to measure major and minor diameters of the cells [75]. The equivalent spherical diameters were determined for the cells such that the volume of the equivalent sphere was the same as that of the ellipsoidal cell with the specified major and minor diameters. The circularity of cells was determined

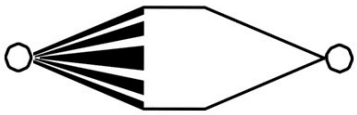

Figure 2.1: Top view of microfluidic flow chamber.

by the following equation,

$$\text{circularity} = 4\pi \frac{A_{cell}}{P_{cell}^2} \tag{2.1}$$

where A_{cell} and P_{cell} are the imaged area and the perimeter of the cell. Circularity equals to one means morphology of cell is a perfect sphere.

2.2.3 Surface Preparation and Microfluidic Chip Design

Substrates used in adhesion experiments were PDMS thin films. Thin films of PDMS were prepared on glass slides (Thermo Fisher, Fisherbrand^{TM} Adhesion Slides). Microscope glass slides were rinsed with deionized water (DI) and acetone and air-dried. PDMS solutions were prepared using a Sylgard 184 silicone elastomer kit (Dow Corning). The base and curing agent ratio was 10:1. A spatula was used to mix base and curing agent and mixture was degassed for 1 h until no bubbles remained. Glass slides were cleaned by wiping with tissue soaked in acetone and then in isopropanol. PDMS solution was spin coated (Specialty Coating Systems. Inc) on glass slides with 1 g per slide, speed was set to 1200 rpm for 25 s. Finally, slides were cured in an oven at 65 °C overnight.

To ensure a constant and laminar flow during the adhesion experiments, a microfluidic flow chip was used. This was provided by the Elvira group in the Department of Chemistry at the University of Victoria, and was based on a slight modification of one of their previous designs [76]. Figure 2.1 shows the diagram of a microfluidic chip. The chamber thickness is 42.5 ± 1 μm and the width of the chamber is 5780 μm. The pillar network was designed to break cell clusters for single-cell attachment in the middle of the chip. There were slight

modifications between the actual chip and the design above. The holes inlet and outlet were punched just beside the chamber and the excess channels were removed to ensure a more smooth flow of cell culture.

Chips were plasma bonded with spin-coated PDMS using air plasma surface treatment machine (Diener ZeptoOne). The power was set to 975 W and the generator was allowed to run for 38 s. The devices were put in the oven immediately after bonding at 60 °C overnight.

In order to compare, a clamped microfluidic device was built up to test adhesion between cells and PDMS surfaces that did not go through plasma treatment. Figure 2.2 shows the design of the device. Instead of plasma bonding, four clamps were used to secure and bond microfluidic chips and PDMS slides. Glass slide was cut to a smaller size (25 mm $\times$ 30 mm) and the PDMS mix solution was spin-coated on it and went over the same procedure above. Chip covered the center of PDMS slides and four clamps were carefully clamped close enough to the edge of microchannels. The leaking test should be run before the actual adhesion experiment.

Four microfluidic chips were injected in water and 5% (w/w) of sodium chloride solution, respectively, and immersed in both solutions for surface treatment purpose. The soaking time length was 30 d. One plasma-treated PDMS slide went through the same soaking procedure above and measured the surface contact angle at day 30 as an experimental control.

2.2.4 Measurements of Contact Angle of Treated PDMS Surface

Four plasma-treated PDMS slides were immersed in water and 5% (w/w) of sodium chloride solution up to 30 d. Contact angle measurements were made by contact angle meter (Holmarc, HO-IAD-CAM-01B) and samples were observed under an optical microscope connected with contact angle meter. Since PDMS slides were immersed in the solution, there were two drying methods to dry the samples: (i) Ambient air dry the

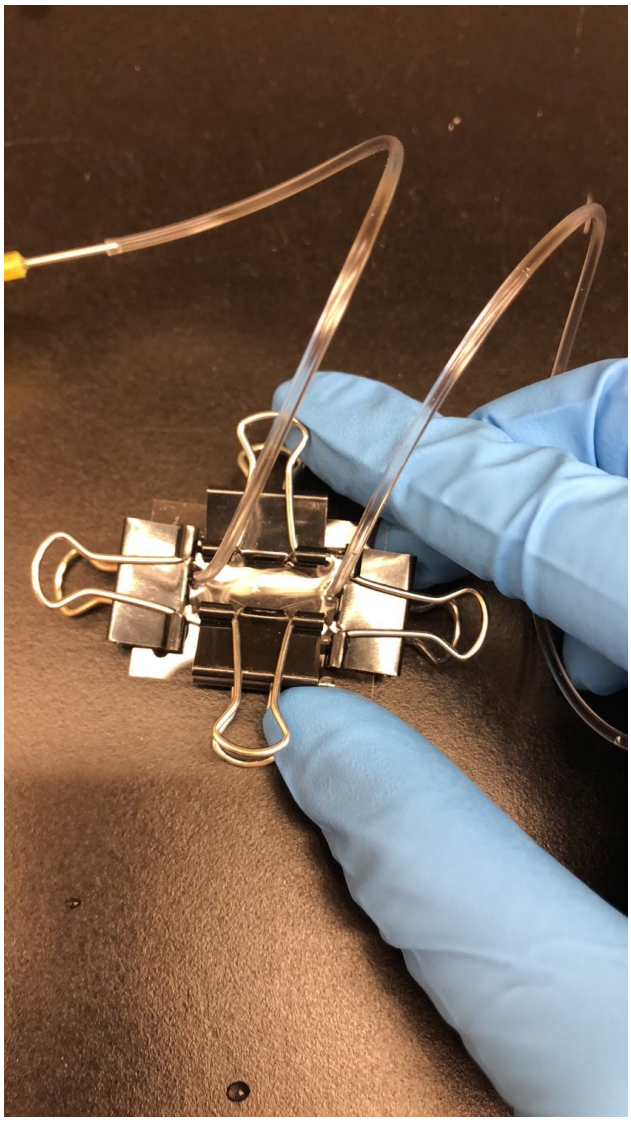

Figure 2.2: Design of microfluidic clamped device.

sample one day before contact angle was measured, (ii) Using compressed nitrogen gas to blow the sample surface just before conducting contact angle measurement. Contact angle measurements were conducted on day 1; day 5; day 10; day 20 and day 30 and were measured for each sample at 5 different locations. Successive droplets of deionized water with 4 μL volume were placed over the slides until contact angle measurements were stabilized. The results presented are the average of at least 10 measurements (two contact angles per droplet) performed with each probe liquid.

2.2.5 PDMS Profilometry Measurements and ATR-IR Spectra

Profilometry measurements of PDMS thin film under different soaking conditions (prepared in section 2.2.3) were performed using stylus profilometer (Bruker, Dektak XT), and the analysis was carried out using the Vision 64 software. Several scratches with average length around 200 μm were made on the prepared substrate using a razor blade. The film thicknesses and surface roughness were obtained from the respective depth profiles. ATR-IR spectra of PDMS thin film under different soaking conditions (prepared in section 2.2.3) were recorded with a OPUS IR spectrometer (Bruker) at a scanning range of 400–4000 cm^{-1}. The ATR-IR measurement was repeated at three locations of the sample.

2.2.6 Adhesion Strength Measurements

Figure 2.3 used for the adhesion tests. A syringe pump (New Era, NE-1000) delivered 500 μL concentrated algal culture through a 2 mL syringe at a high flow rate (1–2 $mL{\cdot}min^{-1}$) for a very short of time, around 10–15 s. This step made sure there is enough single cell attached to the surface at the same time and therefore can be incubated over the same amount of time. The attachment surface was imaged with an inverted microscope Nikon Diaphot-TMD) equipped with a digital camera (Amscope, MD300) and a 4X objective (Nikon, Nikon Fluor 4X) for in situ enumerations of attached cells. The process of detachment was recorded as a video for further analysis. The cells that remained attached after 2 min of a washout with a very low flow rate (30 $\mu L{\cdot}s^{-1}$) were considered

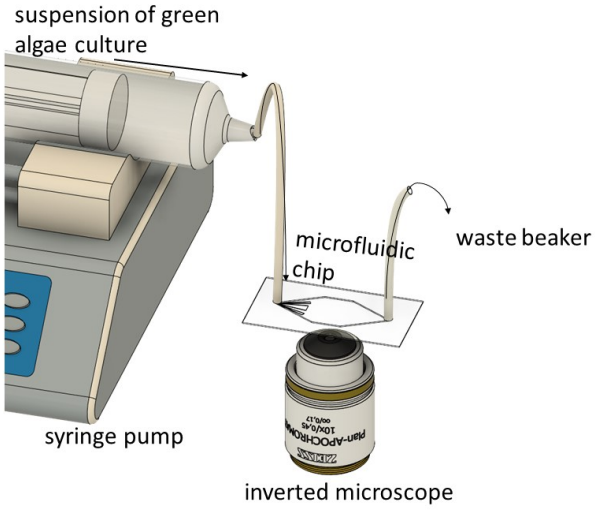

Figure 2.3: Experimental setup for quantification of cell adhesion: 60 mL of syringe filled with BG-11 medium is connected to the inlet of microfluidic chip by tygon tubing with size 0.02 "$\times$ 0.06". The outlet of microfluidic chip is connected with a waste beaker.

to be adhered.

After the loading and washout step, cells were settled on the surface with pre-determined incubation time, ranging from 15 min, 30 min to 1 h. After incubation, cells left on surface were washout with same flow rate, 30 μL corresponding to Re = 0.0960 and $\dot{\gamma}$ = 287 s^{-1}. In order to quantify the adhesion strength, the flow inside the chip was then increased stepwise at various flow rates with increments 200 μL·min^{-1}. The detailed flow rate, Re and $\dot{\gamma}$ for each treatment were listed in Table 2.1. The Re, $\dot{\gamma}$, and the net force due to lift and drag forces acted on cells were also calculated based on equations [77]. Each of the flow rates was maintained for a duration of 30 s.

2.2.7 Wall Shear rate, Lift, Drag and Adhesion force

Essentially, a microfluidic chip is a parallel plate flow chamber that experiences lift and drag forces due to fluid flow [77]. Wall shear rate acting on adhering algae is the main source of fluid that causes cell adhesion [77]. Wall shear rate depends on fluid flow rate, fluid velocity and dimensions of the chamber [77]. Equation 2.2 demonstrated wall shear

Table 2.1: Microfluidics experimental flow rate steps

	1 h	30 min	15 min	15 min salt soaking	15 min deionized water
Initial flow rate (μL·min^{-1})	100	200	200	200	200
Final flow rate (μL·min^{-1})	1900	2400	1400	600	600
Increment (μL·min^{-1})	200	200	200	200	200
Initial *Re*	0.32	0.64	0.64	0.64	0.64
Final *Re*	6.08	7.68	4.48	1.92	1.92
Initial $\dot{\gamma}$ (s^{-1})	956	1910	1910	1910	1910
Final $\dot{\gamma}$ (s^{-1})	18200	22900	13400	5740	5740

rate in a rectangular flow displacement system, respectively [77].

$$\dot{\gamma} = \frac{3Q}{2(h/2)^2 w} \tag{2.2}$$

where Q is the volumetric flow rate in m^3·s^{-1}, h is the depth and w is the width of the parallel plate flow chamber, ρ is the density of fluid in kg·m^{-3}, η is the viscosity of fluid in Pa·s^{-1}. The Reynolds number expressed in equation 1.7.

The main hydrodynamic force generated by the flow on the cell depends on the velocity gradient near the wall [77]. There are three forces acting on adhere sphere cells: shear force, lift force and drag force. Shear force can detach cells mainly due to rolling movement of the cells combined with influence of minor surface roughness and chemical heterogeneities [77]. The shear force is calculated as [77]:

$$F_{\text{shear}} = \mu \dot{\gamma} A_{\text{exposed}} \tag{2.3}$$

where A_{exposed} is the area of the adhering cell as exposed to the flow.

For a fully developed laminar flow in a microfluidic chip, the velocity profile showed in equation 1.8 where H is the vertical distance from the substratum surface to the center of the cell.

The lift force is due to different flow velocity around cells, which act perpendicular to cell-substratum interaction. The lift force is calculated as [78]

$$F_{\text{lift}} = 81.2\mu r^2 (\frac{\dot{\gamma}\rho}{\mu})^{1/2} v(a) \tag{2.4}$$

Table 2.2: Cell morphology of *B. braunii*.

Major diameter	10.9 ± 1.1 μm
Minor diameter	9.79 ± 1.19 μm
Equivalent sphere diameter	10.3 ± 0.9 μm
Circularity	0.815 ± 0.0524 μm

where $v(a)$ is the flow velocity over the substrata at a vertical distance equal to the radius of the cell. However, lift force is usually considered too little to lead detachment [77].

Viscous drag forces generally cause rolling of adhering cell, is expressed as [78] :

$$F_{\text{drag}} = 1.70096\pi\mu r v(a) \tag{2.5}$$

2.3 Results and Discussions

2.3.1 Properties of *B. braunii* and PDMS surfaces

Table 2.2 presents the morphological properties of the *B. braunii* and Figure 2.4 demonstrates one example of imaging processing and morphology data collection. There were 52 individual cells collected. The results indicate that *B.braunii* has circularity close to one. The equivalent spherical diameter was used as the size parameters of algal cells in the subsequent modeling studies.

In this study, water contact angle measurements are performed to assess the hydrophobicity of the surfaces before and after salt solution and DI water exposures. Table 2.3 summarizes the experimentally measured PDMS surface contact angles under two different soaking conditions with two different drying methods. The results indicate there is no significant difference between plasma-treated PDMS surface and plasma-treated PDMS surfaces exposed to salt solution or DI water for 30 d. All the static contact angles close to 110°C, consistent with many literature values. Besides, contact angles measured with two different drying methods show no significant difference as well. This demonstrates the hydrophobicity of the PDMS surface does not change, even though the contact angles were measured right after the surface dried. Chen *et al.* claimed

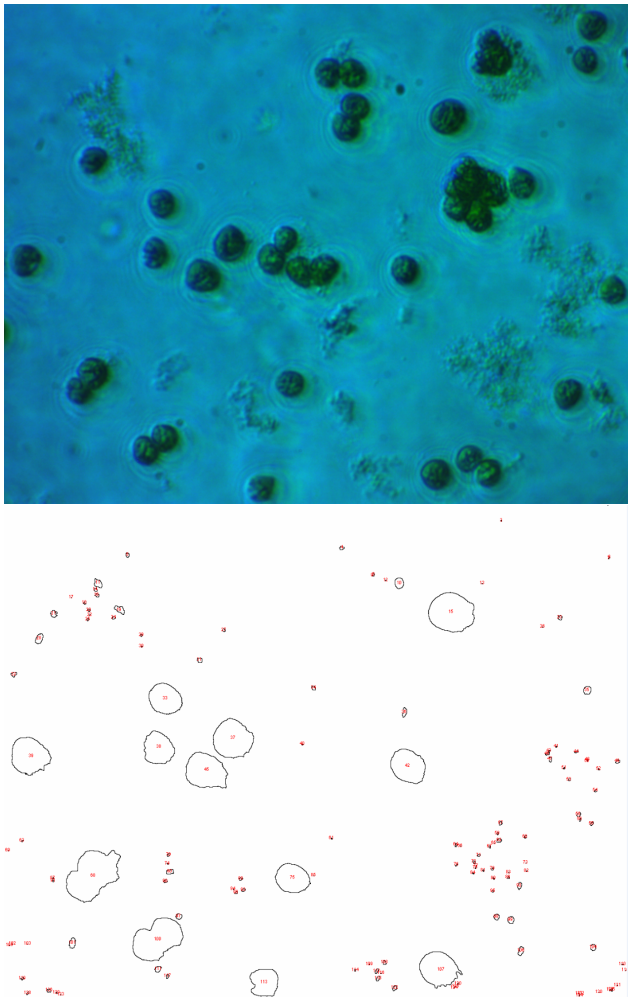

Figure 2.4: The example of cell morphology of *B. braunii* and it's ImageJ processing.

Table 2.3: Contact angle measurements of PDMS

Days	1	5	10	20	30
Salt solution soaking with air dry overnight (°)	106 ± 6	104 ± 3	107 ± 6	105 ± 5	109 ± 6
Salt solution soaking with immediate dry (°)	105 ± 4	103 ± 5	106 ± 6	104 ± 5	108 ± 2
Distilled water soaking with air dry overnigh t(°)	106 ± 6	101 ± 7	100 ± 5	111 ± 3	111 ± 5
Distilled water soakingwith immediate dry (°)	105 ± 5	95 ± 3	98 ± 4	106 ± 6	110 ± 3

that the rate of the hydrophobicity recovery slowed down when plasma-treated PDMS placed into a high dielectric constant environment (salt solution and water) compared to a low dielectric constant environment (air), indicating that the aqueous environment was favorable hydrophilic functional groups (Si–OH) and tent toward the surface instead of bulk [79]. However, their outcomes showed that hydrophobicity recovery was faster when PDMS exposed to 0.14 M NaCl solution, although the dielectric constant of water and salt solution was very similar [79]. Bausch *et al.* found that contact angles of non-treated PDMS surface decreased to 85–90° after the surfaces exposed to DI water and salt solution for 14 d [80]. Our results showed that there were some fluctuations of contact angle measurements of the water-exposed surface on day 5 and day 10, however, the wettability was recovered back to 110° on day 30.

We applied a profilometry technique to evaluate each treated sample roughness. Table 2.4 shows roughness values of all pristine and treated surfaces were very similar, mirroring these surfaces' wettability behavior. Maji *et al.* measured that the average surface roughness of pristine PDMS was about 650 ± 100 Å [81], the thickness of their film was about 550 μm. The surface roughness is related to the thickness of the PDMS film. The thicker the film is, there are more variations in the surface roughness and the rougher the surface is.

The ATR-IR spectra (Figure 2.5) of pristine, salt solution exposed and DI water exposed PDMS surfaces illustrate that surfaces show no significant difference among the three treatments. IR peaks at 789–796 cm^{-1} are CH_3 rocking and Si–C stretching in Si–CH_3, peaks at 1020–1074 cm^{-1} are Si–O–Si stretching, and peaks at 2950–2960 cm^{-1} are

Table 2.4: Roughness values obtained from profilometry analysis.

	Pa (arithmetic average)	Pq(root square average)
Pristine PDMS	18.4 ± 12.3 nm	21.9 ± 13.2 nm
30 days salt solution exposure PDMS	14.5 ± 2.5 nm	20.2 ± 4.5 nm
30 days DI water exposure PDMS	42.1 ± 9.8 nm	55.3 ± 9.0 nm

asymmetric CH_3 stretching in Si-CH_3. There is no evidence to show that water stretch (OH group) exits at any wavenumber. The ATR-IR results suggest that no water molecules were remained or trapped in the surfaces.

2.3.2 Microfluidic chip flow experiments

Figure 2.6 presents the percentage of the initial number of cells that remained attached over PDMS as a function of wall shear rate and adhesion force with different incubation times during the microfluidic chip flow experiments. The number of cells remaining was collected by software developed by our group for the control of a NE-1000 syringe pump as well as the analysis of videos of experiments monitoring the cell adhesion. Based on these results, the adhesion strength was smallest for cells with an incubation time 15 min and increasing with longer incubation time. The figure demonstrates that when cells were incubated in a microfluidic device for 1 h, $27 \pm 4\%$ of initial adhered cells were removed after a wall shear rate of 20000 s^{-1} corresponding to a net force of 4.64×10^{-8} N acting on the cells. For 30 min incubation time, $54 \pm 15\%$ of initial adhered cells were removed after a wall shear rate of 21000 s^{-1} corresponding to a net force of 4.19×10^{-8} N acting on the cells. For the shortest incubation time, 15 min, $86 \pm 6\%$ of initial adhered cells were removed after a wall shear rate of 13400 s^{-1} corresponding to a net force of 2.43×10^{-8} N acting on the cells.

These results indicate that the shorter the incubation time, the smaller the cell adhesion strength to the PDMS surface. *B. braunii* is known as a significantly higher oil production compared to other microalgae. Kim showed that there was a growth/biomass increase and

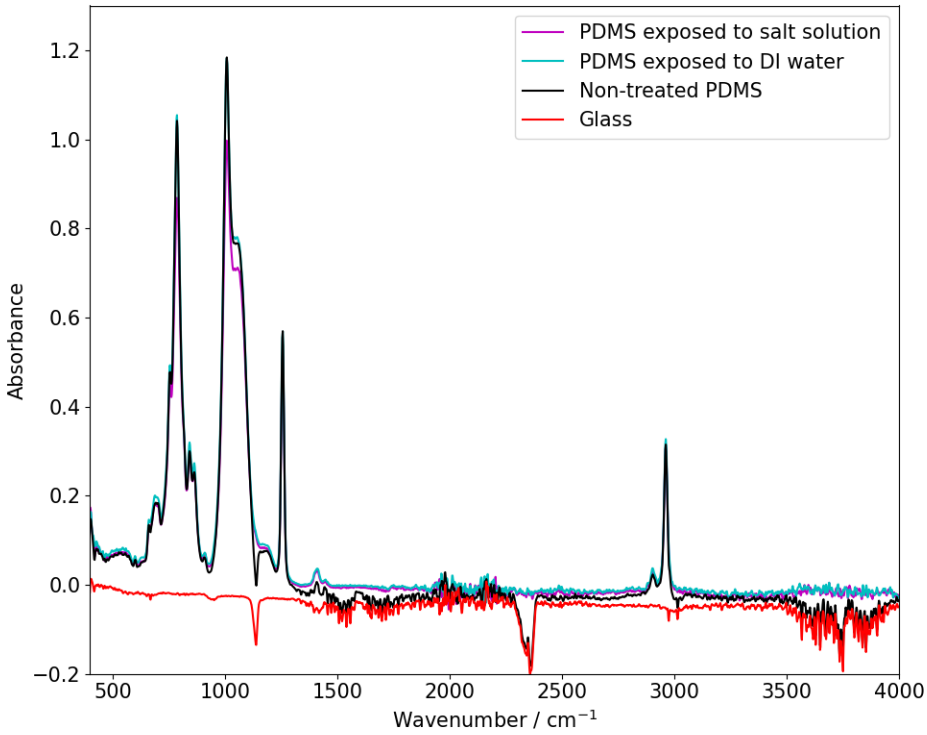

Figure 2.5: ATR-IR spectra of pristine, salt solution exposed and DI water exposed PDMS surfaces.

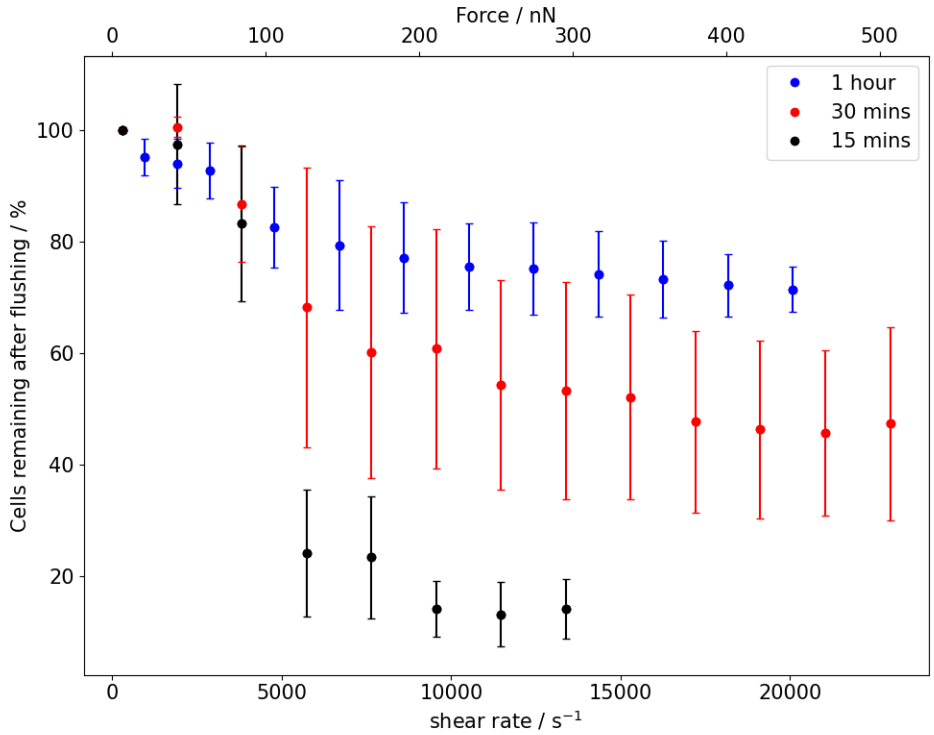

Figure 2.6: Ratio of *B. braunii* remained attached over PDMS with selected incubation time (1 h, 30 min and 15 min) as function of shear rate and force.

oil production during the first 8-hour incubation in the photobioreactor array, regardless of light intensity control [73]. Their results may indicate that in our experiments, *B. braunii* cells were keeping producing hydrophobic EPS during the incubation time, the longer the incubation time was, the more EPS produced. The accumulated hydrophobic EPS mixed with cells, leading to stronger adhesion onto surfaces. Thus, it was found the adhesion strength of *B. braunii* is dependent on the length of cell-adhering time.

Figure 2.7 presents the percentage of the number of cells that remained attached over the PDMS surface with and without plasma bonding as a function of wall shear rate and adhesion force. Compare to the plasma bonding PDMS chip, almost 90% of initial adhered cells were removed after a wall shear rate of 13400 s^{-1} corresponding to a net force of 2.43×10^{-8} N acting on the cells in the bulldog clip chip. The percentages at highest shear rate were close under both conditions, with 3% higher for cells remaining on plasma bonding chips. However, at the initial shear rate, plasma bonding chips showed a relatively

higher percentage compared to the non-plasma bonding chips. At shear rate 2000 s^{-1}, the difference was near to 30% between two conditions.

Several possible explanations can be stated here. Firstly, as mentioned, the flow cell was created by assembling the chip and substrate by using clamped microfluidic chips. This does deform the PDMS walls, leading to a slight decrease in the channel width as compared to the plasma bonding channel. The flow velocity inside the channel is very sensitive to the channel width, therefore, a slightly higher flow velocity could be created due to the deformation. Secondly, air plasma caused surface structural modification. Chen *et al.* found that PDMS with 1.3 mm thickness showed a significant contact angle drop after 2 min air plasma treatment. The surface became hydrophilic right after air plasma treatment. However, the plasma treatment induced hydrophilicity was gradually lost with time. After 30 d of exposure to air, the contact angle of the PDMS surface was recovered back to 70° [79]. On the other hand, Ginn and Steinbock found that it only took 400 min to recover the PDMS surfaces from 15° to 80° after a 25 s oxygen plasma exposure. Maji *et al.* showed that the contact angle of oxygen plasma-treated PDMS (30 s at 18 W power, 550 μm thickness) was recovered back to 104° after 250 h (10 d) [81]. Plasma bonding is a necessary and inevitable step in the fabrication of the microfluidic chip. To minimize its effect, all the surface characterization experiments as well as flow cell adhesion experiments were using a 10-day old plasma treated PDMS. The contact angle results in section 2.3.1 showed that after 10 d of hydrophobicity recovery, the initial contact angle measurement of the plasma-treated surface was 106°. The possible mechanisms of hydrophobic recovery include condensation of the induced silanol groups, the reorientation or diffusion of polar groups into the PDMS bulk, and the migration of untreated, low molecular weight polymeric chains to the PDMS surface while Si-OH bonds toward the bulk at room temperature [79]. Ozkan *et al.* found that to minimize biofouling in aquatic systems, hydrophobic microalgae such as *B. braunii* resulted in weaker adhesion strength onto hydrophilic surfaces [62]. Plasma treated surfaces should become hydrophilic and

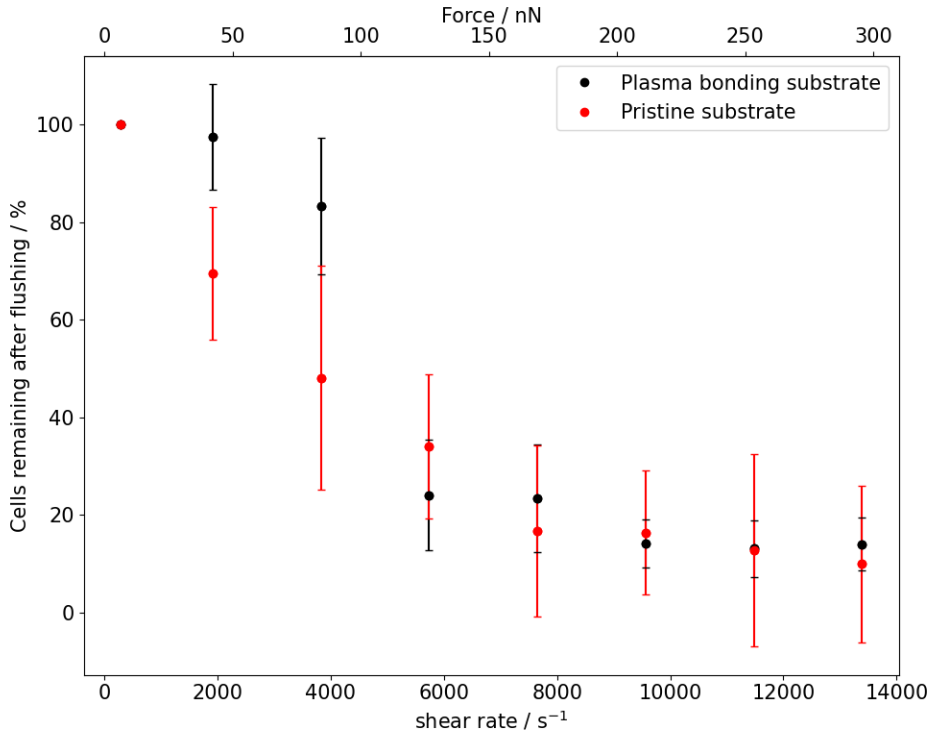

Figure 2.7: Ratio of *B. braunii* remained attached over PDMS with and without plasma bonding as function of shear rate and force.

cells should be easier to remove. Figure 2.7 illustrated the opposite outcomes. Therefore, the first reason could be more possible to explain these outcomes. The effect of plasma bonding on the surface structure is possible but minor.

Figure 2.8 presents the percentage of the number of cells that remained attached over PDMS as a function of wall shear rate and adhesion force under different soaking conditions during the microfluidic chip flow experiments. The plasma bonding chips were used. The results show that soaking treatment to PDMS surface made cell adhesion strength even smaller. The end point percentages were close under both soaking conditions, $10 \pm 5\%$and $13 \pm 9\%$ of the cells remained attached with shear rates of 5700 s^{-1} for soaking in salt solution and deionized water, respectively. While at the same shear rate, the percentage of cells remaining on the surface was 24% under non-soaking condition. At the initial shear rate (1900 s^{-1}), the percentage of cells remaining on the surface under

salt solution soaking condition was much lower than the percentage under water soaking condition. Cells were barely removed ($99 \pm 1\%$ remaining) at 1900 s^{-1} under water soaking condition while only $14 \pm 6\%$ cells remained at the same rate under salt solution soaking condition.

In conclusion, in the same amount of incubation time, *B. braunii* cells were least adhesive onto salt solution exposed PDMS surfaces, then onto DI water exposed PDMS surfaces. *B.braunii* cells showed the strongest adhesion strength onto pristine PDMS surfaces. Ozkan *et al.* concluded that the hydrophobic algae such as *B. braunii* were less adhesive to hydrophilic coatings [63]. Therefore, the PDMS surface exposed to salt solution was least hydrophobic; the PDMS surface exposed to salt solution was less hydrophobic than pristine PDMS. One possibility was surface hydrolysis. However, PDMS surface hydrolysis usually happened at high temperatures. West stated that activation energy for hydrolysis of the Si–O bond was found to be +23 Kcal·mol^{-1}, and there was no observation of hydrolysis up to 350 °C [82]. Therefore, surface hydrolysis of treated PDMS films under ambient temperature was less likely. However, silicone surface chemistry currently is a highly controversial due to the possibile auxiliary influences. The long-term effect of saline solution exposure was unknown. It is noticeable that all PDMS substrates in this set of experiments went through plasma treatment. Although the contact angle measurements in section 2.3.1 showed little change of surface hydrophobicity, it was possible that the surface was not fully recovered and some polar functional groups (Si–OH) remained on the surfaces. Studies showed that PDMS surfaces are very sensitive to the presence of trace hydrophilic species. Bausch *et al.* stated that the plasma-treated Medical Grade PDMS showed a slower hydrophobicity recovery rate when it was stored in an aqueous environment (water and seawater) [80]. Since hydrophilic groups prefer the higher dielectric constant environment, immersing such surfaces in an aqueous solution for 30 d creates a favorable environment for the silanol group, inducing more silanol groups from bulk PDMS to the surface. Our results demonstrated that cells were least adhesive

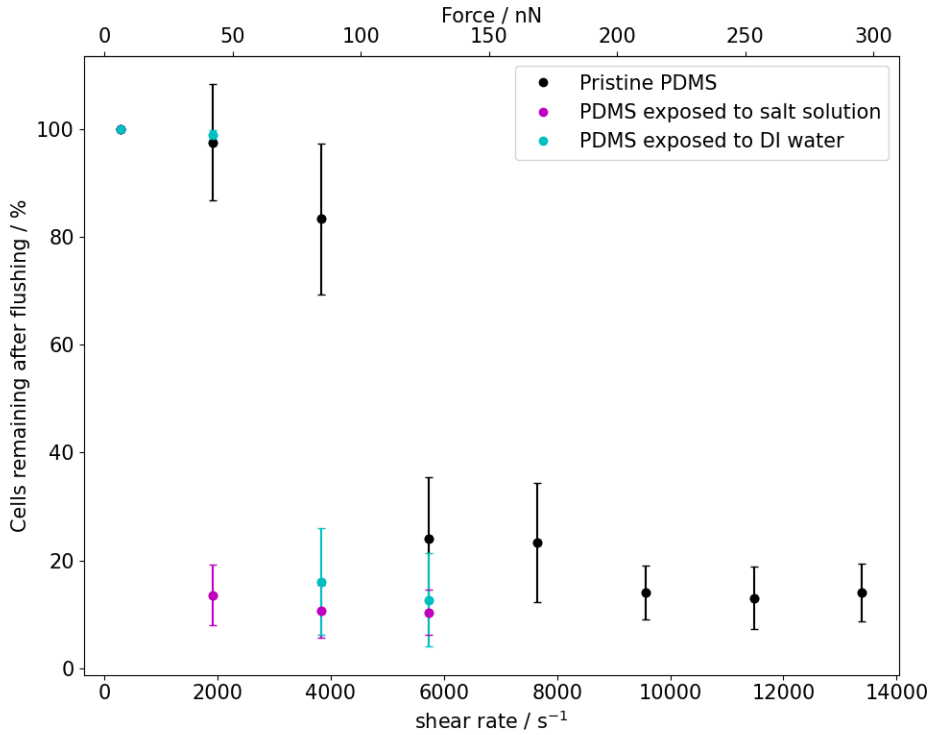

Figure 2.8: Ratio of *B. braunii* remained attached over PDMS under non-soaking condition, soaking in salt solution for 30 d and soaking in deionized water for 25 d as function of shear rate and force.

onto salt solution exposed PDMS surfaces, indicating such surfaces had most polar groups generated on the PDMS surface tend to orient toward salt solution.

Chapter 3

Quantifying the Adhesion of Diatoms onto Polydimethylsiloxane Surface

3.1 Introduction

Diatoms are ecologically important phytoplankton because of their role in primary production, supporting food webs, carbon fixation, and nutrient biogeochemical cycles. However, individual taxa can have a variety of negative effects. For example, *Pseudonitzschia sp.* are often responsible for harmful algal blooms causing toxicity in shellfish, marine mammals, and humans [83]. *Thalassiosira rotula* (*T. rotula*) is one species of marine diatoms. Cells are widely discoid and connected in a chain by a thick bundle of threads. Threads extend from a cluster of central strutted processes. Generally, the diameter of the cell is ranging from 8 μm to 60 μm, and the thickness of the cell is ranging from 5 μm to 20 μm. It is a commonly-occurring diatom that can dominate phytoplankton assemblages across diverse marine habitats and hydrographic environments. The geographic distribution of this species located in the Eastern and Western Pacific and Western Atlantic [84]. For seasonal distribution, diatoms are abundant during spring. Optimal growth conditions in nature are estimated to be around 14 °C with a light intensity of 2000–3000 lux and salinity of 20–33 ppt. Furthermore, the researchers found that such diatoms release polyunsaturated short-chain aldehydes (PUA). The activation of oxylipin-based chemical defense in the diatom *T. rotula* is initiated by phospholipases that act immediately after cell damage.

Thalassiosira rotula is a pelagic diatom found throughout oceanic and coastal waters across a wide latitudinal range, $\approx 60^{\circ}$N–43°S [85] and is capable of growing under broad ranges of temperature, light, and salinity. [86,87] The genus Thalassiosira is globally one of the most abundant diatoms, representing $\approx 13\%$ of total diatom biomass, and T. rotula specifically is among 43 identified species that account for 90% of global diatom biomass. [88] Such a cosmopolitan diatom is therefore well-suited to laboratory studies on diatoms that seek to apply their results to the broader diatom community.

Similar to the last chapter, in this chapter, we investigate the adhesion strength between *T. rotula* and PDMS surface by using a flow cell chamber with relatively low shear stress, since diatoms are much less sticky than benthic green algae. The adhesion force was measured for surfaces that (i) without any stress (pristine), (ii) under pure water exposure, and (iii) under salt solution exposure.

3.2 Materials and Methods

3.2.1 Diatom Culturing and Sample Preparation

Thalassiosira rotula (CCMP3362) was obtained from the National Center for Marine Algae and Microbiota, Bigelow Laboratory. The culture was maintained in exponential growth through semi-continuous batch culturing in an enriched seawater medium, [89] at 14 °C, under 65 μmol photons$\cdot$m$^{-2}\cdot$s^{-1} on a 13:11 light to dark cycle [90]. At the time of adhesion experiments, diatoms were subsampled from the parent cultures near the end of the exponential phase, prior to a maintenance dilution at the point when cell densities were highest. The morphological characteristics of diatoms were quantified from images obtained with an imaging multi-mode reader (Cytation 5, BioTek Instruments, Inc) using ImageJ to measure the diameter and thickness.

3.2.2 Characterization of Morphological Properties of Diatoms

Morphological properties of cells were quantified based on their images obtained with cell image multi-mode reader [75]. There are two morphology models used in diatom cells: equivalent sphere and flat circular disk. The equivalent spherical diameters were determined for the cells such that the volume of the equivalent sphere was the same as that of the cylindrical cells with the diameters.

3.2.3 Surface Preparation and Flow Cell Chamber Hardware Design

PDMS thin films with two different thickness were prepared in these experiments. Pristine/treated PDMS covered slides are prepared in the same way as section 2.2.3, resulting in a thickness of 10 μm. The PDMS solution was spin-coated with speed and was set to 5000rpm for 5 min Finally, slides were cured in an oven at 80 °C for 4 h. This process resulted in a PDMS thin film with 300–400 nm thickness. Since microfluidic chips were not involved in this chapter, slides did not go through the plasma bonded procedure.

A parallel-plate flow cell chamber was designed in this chapter to test adhesion strength between diatom cells and pristine/treated PDMS surfaces. The height and lateral dimensions of the flow channel were set according to a laser-cut rubber spacer, the channel had a height of 0.8 mm, and width of 0.8 cm in its central section. The exact dimension of the spacer was adapted from Ref. 62, shown in Figure 1.2. this rubber layer was sandwiched between the PDMS-coated glass slide and a clean glass slide and pressed together inside a laser-cut acrylic mount that was held together with bolts. The mount was designed to fit onto an opening in the stage of an inverted microscope (Nikon Diaphot-TMD). Tygon tubing with 3 mm ID was used to connect the flow cell outlet to a syringe pump (New Era NE-1000), and outlet to a waste beaker. The microscope was fitted with a digital camera (Amscope MD300), connected to a computer via USB.

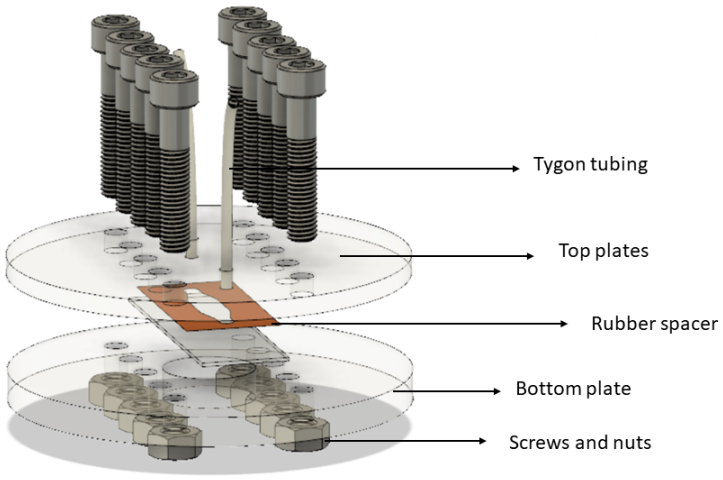

Figure 3.1: Diagram showing the various layers and dimensions of the channel.

3.2.4 Adhesion Strength Measurements

The cell culture was suspended in a falcon tube which was set up beside the microscope stage. The detailed experimental setup is shown in Figure 3.2. The syringe pump was used to deliver the diatom suspensions from the falcon tube to the flow cell chamber. The diatom suspensions initially were delivered into the chamber at a flow rate of 0.005 mL·min^{-1} for 2 min. After 2 min loading in the process, cells were left on the surface undisturbed for 15 min or 20 h. After incubation, cells left on the surface were washed out using the same flow rate, shear rate $\dot{\gamma} = 0.0222$ s^{-1}. A surface area of 0.0152 cm^2 was imaged and recorded a video using the digital camera. The cells remaining on the surface after 2 min of washing were considered to be adhered. In order to quantify the adhesion strength, the flow inside the chip was then increased in a stepwise manner. The detailed flow rate, *Re* and $\dot{\gamma}$ for each condition were listed in Table 3.1. Each of the flow rates was maintained for a duration of 30 s.

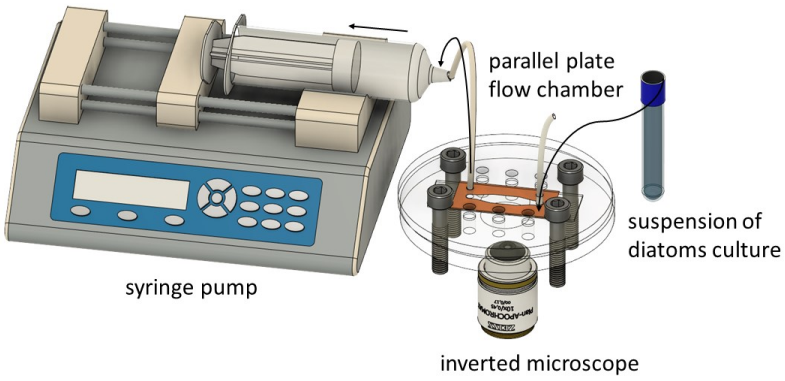

Figure 3.2: Experimental setup for quantification of cell adhesion: 60 mL of empty syringe was connected to the outlet of flow cell chamber by PVC tubing with size 0.25" ×0.125". The inlet of flow cell chamber was connected with the diatoms culture suspension by the PVC tubing.

Table 3.1: Flow cell chamber experimental flow rate steps

	15 min incubation 10 μm PDMS	15 min incubation 300 nm PDMS slides	20 h incubation 300 nm PDMS slides
Initial flow rate (mL·min^{-1})	0.02	0.05	0.05
Final flow rate (mL·min^{-1})	0.56	0.85	0.85
Increment (mL·min^{-1})	0.02	0.05	0.05
Initial *Re*	0.0432	0.111	0.111
Final *Re*	1.21	1.83	1.83
Initial $\dot{\gamma}$ (s^{-1})	0.44	1.11	1.11
Final $\dot{\gamma}$ (s^{-1})	12.4	18.9	18.9

3.2.5 Drag Force Calculation for *T. rotula*

For a fully developed laminar flow with a very low flow rate between two parallel plates, fluid inertia is negligible compared with viscous forces. This type of flow is Stokes flow or creeping flow regime. The Saffman lift force and Stokes drag force are the two forces acting on adhered spherical micro-organism in parallel plate flow chambers. At very low Reynolds number, both lift and drag force are independent of Reynolds number [77]. But are generally lift force is considered too weak to cause microbial detachment [77]. Therefore, in this study, we focus on the fluid drag force exerted on diatom cells. Most researches about micro-organism cell adhesion used spherical shape cells to estimate adhesion force since spherical symmetry (symmetry around a point) numerically is easier to solve than other azimuthal symmetry (symmetry along an axis). There are two geometry models we can apply to *T. rotula* cells. Based on the morphology study, the actual shape that cells closed to is a flat circular disk. Therefore, the drag force of circular flask disk in the flow cell chamber could be calculated by equation 1.16, with $F_{d\infty}$ is the drag force on the flat disk when moving in the unbounded medium, shown in Table 1.1 and k was chosen under the condition of single plane walls, shown in Tabel 1.2.

3.3 Results and Discussions

3.3.1 Properties of *T. rotula*

Table 3.2 presents the morphological properties of the *T. rotula* and Figure 3.3 demonstrated one example of imaging processing and morphology data collection. There were 70 individual cells be collected. For flat circular disk model, the results indicate that average major diameter was 24.9 ± 7.9 μm; the average thickness was 15.5 ± 2.9 μm. For sphere model, the equivalent spherical diameter 12.2μm.

Table 3.2: Cell morphology of *B. braunii*.

Major diameter	24.9 ± 7.9 μm
Thickness	15.6 ± 2.9 μm
Diameter/thickness ratio	1.60
Equivalent radius	12.2 ± 0.02 μm

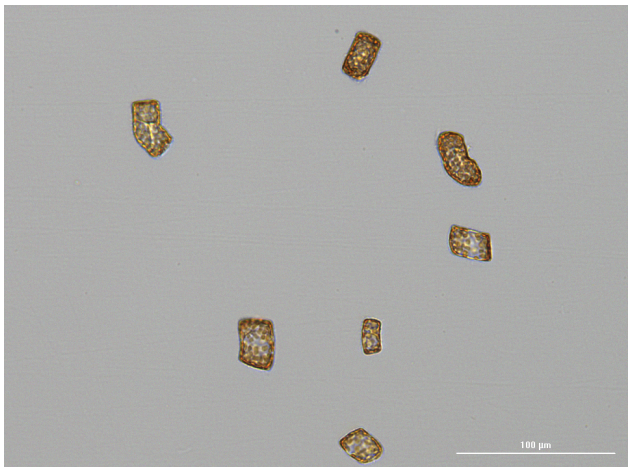

Figure 3.3: Cell morphology imaging processing.

3.3.2 Flow Cell Experiments

Figure 3.4 presents the percentage of the number of cells that remained attached over PDMS as a function of wall shear rate and adhesion force under different soaking conditions during the flow experiments. The results show it took less force to remove the adhered cells on PDMS surfaces under soaking conditions compared to surfaces under non-soaking conditions. Due to the experimental error, the shear rate stopped ramping up at 7.56 s^{-1} for Figure 3.4. At this shear rate, there was $33 \pm 12\%$ of cells remaining on the surface under non-soaking condition. However, during the same shear rate, the percentages of cells remaining on the surface under both soaking conditions were much smaller, which were $13 \pm 7\%$ for salt solution soaking conditions and $17 \pm 13\%$ for deionized water soaking condition. This percentage dropped to $15 \pm 8\%$ for non-soaking conditions till the shear rate ramp up to 12.4 s^{-1}.

Although no defensive conclusion appears the hydrophobicity/hydrophilicity of the cell wall of the *T. rotula* specifically, some studies showed that fouling diatoms (*Navicula*

incerta, *Amphora coffeaeformis* var. perpusilla (Grunow) Cleve, *Craspedostauros australis* Cox and *Navicula perminuta* Grunow) had a stronger adhesion strength onto PDMS elastomer compared adhesion strength onto glass or acid-washed glass [91, 92]. The stronger adhesion strength between diatoms and PDMS surface is determined by macromolecules such as exopolymeric mucilage on the diatoms cell surface. Such substances were produced by diatoms over time and favor to accumulate on a low surface energy surface, which is PDMS [92]. The results of Figure 3.4 demonstrates the same trend with the results in figure 2.7. The PDMS surfaces were not treated with air plasma in these experiments. Therefore, the possibility of polar group reorientation was less likely in this case. However, the bulk PDMS may contain hydrophilic contamination such as platinum complex catalysts and polymerization initiator residues. During the soaking in aqueous solutions, these species may migrate to the surface. The other possibility is water penetration. Although several studies demonstrated that water penetration or swelling rate of PDMS is small enough that it can be neglected [93, 94], other papers illustrated some indirect evidence of water penetration into PDMS. Zheng *et al.* found that there was the evaporation of water from the droplets inside the microfluidic channel through PDMS, the water evaporation increased the protein concentration in the droplets over time [95]. Concerning water penetration of surfaces, some water molecules could be trapped near the PDMS-liquid interface. Ions in the bulk solution may alter the water molecule orientations on PDMS surfaces permanently and more polar groups re-orient towards surface after 30 d incubation.

Figure 3.5 demonstrated the percentage of the number of cells that remained attached over PDMS as a function of wall shear rate and adhesion force for different incubation time during the flow experiments. The thickness of the spin-coated PDMS film was 400 nm. The trends line for both conditions were similar. At the highest shear rate in this experiment, 18.9 s^{-1}, there were $21 \pm 20\%$ of cells remaining on the surface when cells incubated for 20 h and only $6 \pm 1\%$ of cells remaining on the surface when cells incubated for 15 min.

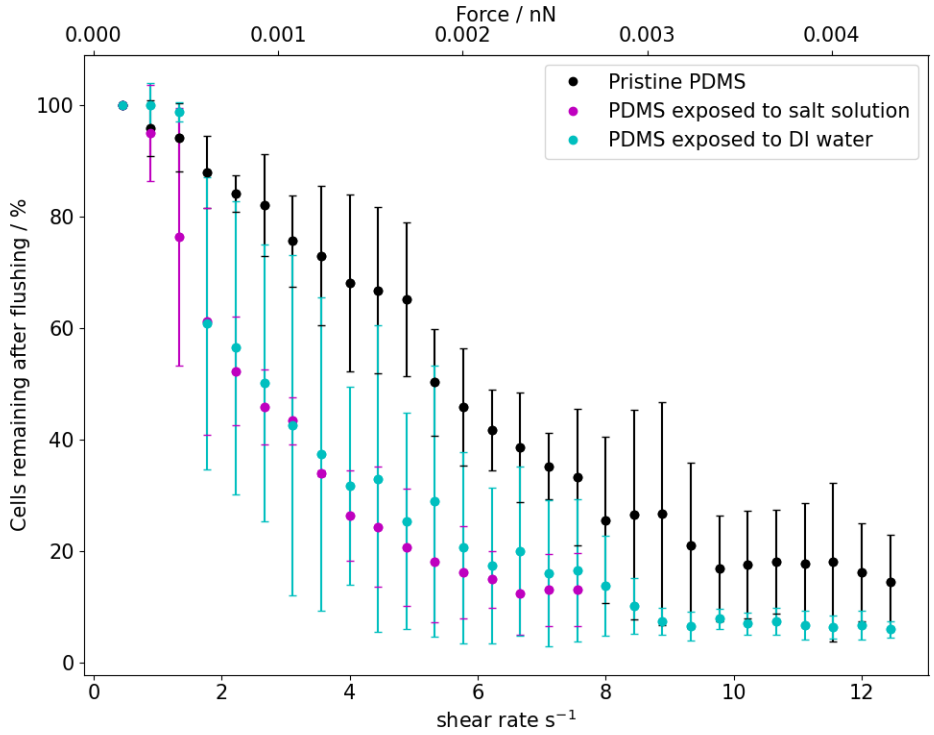

Figure 3.4: Ratio of *T. rotula* remained attached over PDMS under non-soaking condition, soaking in salt solution for 30 d and soaking in deionized water for 30 d as function of shear rate and force.

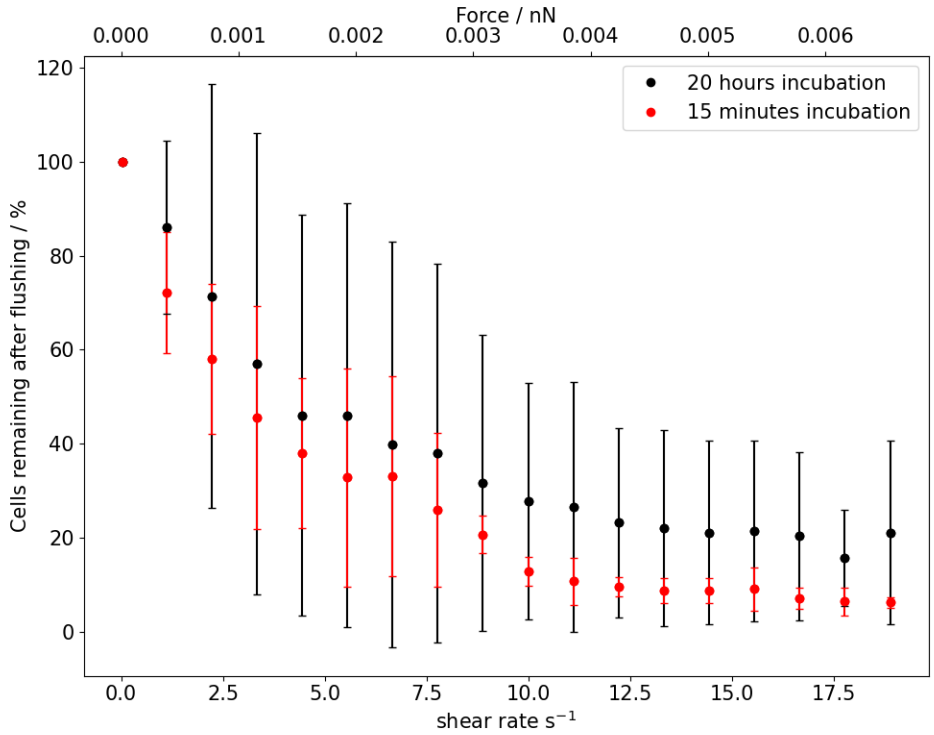

Figure 3.5: Ratio of *T. rotula* remained attached over PDMS with pre-determined incubation time (20 h and 15 min) as function of shear rate and force.

Among all the shear rate increments, the percentage average values for 15 min incubation time were lower to the percentage average values for 20 h. However, the two value's error bars overlapped to each other, which made two experiments have no significant difference. The data points of 20 h incubation experiment had much larger error bar, indicated an increased variability of this data on the surface. A small increase in adhesion force with incubation time has been reported for other diatom species, and has been attributed to enhanced secretion of extracellular polymeric substances [96]. For our *T. rotula*, considering that the half life is ≈ 0.8 d^{-1} h and the cell division is not synchronized, we expect only minor differences with respect to incubation time. Considering the translation of this finding to the silicone insulator biofouling problem, our results indicated that newly adhered algae from an ocean spray are just as difficult to remove as cells that have been in contact with the surface for approximately one day.

Chapter 4

Conclusions

4.1 Summary of Work

In conclusion, cell to PDMS interactions of benthic and pelagic algal species were studied with pristine, DI water exposed and salt solution exposed surfaces. Two different types of flow cells, microfluidic chips, and lab-built flow cell chamber, were employed for our studies to determine critical parameters controlling the adhesion strength of microalgal cells. The benthic freshwater species *B. bruanii* has 50000 times stronger adhesion force than the ocean pelagic species *T. rotula*. The results showed that both cells experienced the highest adhesion strength onto pristine PDMS surfaces, the adhesion was less onto DI water exposed PDMS surfaces; there was a least adhesion strength between both cells with salt solution exposed PDMS surfaces. Three methods (water contact angle measurement, profilometry, and ATR-IR) were used to characterize PDMS surface properties. None of these methods showed any trace of hydrophilic species, such as hydroxyl group or silanol group. None of these methods indicated a surface structural change.

The hypothetical mechanisms based on current results could be:

1. Due to the air-plasma treatment, the surface hydrophobicity was not fully recovered. The aqueous solution created a higher dielectric constant environment to silanol groups, and induced more silanol groups from bulk PDMS to the surfaces. The contact angle measurements of plasma treated surfaces remained hydrophobic, which

constantly around 110°.

2. The previous mechanisms could be possible to explain the results in chapter 3. Although PDMS surfaces in this chapter did not go through plasma treatment, the hydrophilic contamination such as platinum complex catalysts and polymerization initiator residues could also migrate to the surface.

3. Water molecules penetrate through PDMS. Some water molecules were adsorbed on the PDMS surface. Ions in the bulk solution altered the water molecule orientations on PDMS surfaces and polar groups re-oriented towards the surface after 30 d of incubation. ATR-IR spectrum shows no evidence of the existence of the water molecules. On the other hand, ATR-IR may not be sensitive enough to observe the such tiny amount of trapped water molecules on the PDMS surfaces.

Since the results of contact angle measurements and comparison adhesion experiments (plasma bonded chip and clamped microfluidic device) indicated plasma treatment had minor effect to the surface, the second and third hypothetical mechanisms are more likely to contribute different cell-substrate adhesion strength. However, current study does not have enough experimental results to support either of the mechanisms.

4.2 Future Work

Although our experimental results showed aqueous solution exposed PDMS surfaces were less adhesive to microalgal cells compared to pristine PDMS surfaces, future directions of this work could aim to further investigate the surface energy of solution-exposed PDMS. DLVO and XDLVO approaches were adopted by many studies to investigate cell-substrate interactions. In the XDLVO approach, microbial adhesion is balanced between van der Waals, electrostatic interaction energy, and acid-base interaction energy [78]. In the future research, total surface free energy and the surface potential of *B. braunii* and *T. rotula* cells and treated-PDMS surfaces could be obtained experimentally. The surface properties

results can be used in XDLVO approach to understand electron-donating and electron-accepting interactions in bulk solutions and to calculate the free energy of cohesion between cells and surfaces. This can provide a quantitative information about how ions interact with the surface polymer. To understand the subtle surface structural changes, surface-specific nonlinear vibrational spectroscopy could be used to study the surface conditions under different bulk environments. Sum-frequency generation spectroscopy can quantitatively investigate how environmental interfaces influence the algal cell adhesion. Further analysis of sum-frequency generation spectroscopy measurements onto water and salt solution exposed PDMS surfaces could be done to understand interfacial water and methyl group orientations.

References

[1] Dobosz, K. M.; Kolewe, K. W.; Schiffman, J. D. *Front. Microbiol.* **2015,** *6,* 196–196.

[2] Callow, M. E.; Callow, J. A. *BIOL.* **2002,** *49,* 10–14.

[3] Gordon, D. P.; Mawatari, S. F. *Atlas of Marine-fouling Bryozoa of New Zealand Ports and Harbours;* New Zealand Oceanographic Institute: Wellington, 1992.

[4] Ouyang, Y.; Zhao, J.; Qiu, R.; Hu, S.; Zhang, Y.; Wang, P. *Colloid Surf. A* **2018,** *559,* 297–304.

[5] Davidson, I. C.; Brown, C. W.; Sytsma, M. D.; Ruiz, G. M. *Biofouling* **2009,** *25,* 645–644.

[6] Chan, F. T.; MacIsaac, H. J.; Bailey, S. A. *Mar. Biol.* **2016,** *163,* 250.

[7] Yang, S.; Jiaa, Z.; Ouyanga, X.; Bai, H.; Liu, R. *Electr. Power Syst. Res.* **2018,** *163,* 626–637.

[8] Little, B. J.; Lee, J. S.; Ray, R. I. *Electrochim. Acta* **2008,** *54,* 2–7.

[9] Talebian, N.; Doudi, M.; Kheiri, M. *J. Sol-Gel Sci. Technol.* **2014,** *69,* 172–182.

[10] Fogg, G. E. *Bacteriol. Rev.* **1956,** *20,* 148–165.

[11] Quagliarini, E.; Gianangelia, A.; MarcoD'Orazioa,; Gregorinia, B.; Osimanib, A.; Aquilantib, L.; Clementib, F. *CONSTR BUILD MATER* **2019,** *199,* 396–405.

[12] Rossi, F.; De Philippis, R. *Life* **2015,** *5,* 1218–1238.

[13] J.Schnurr, P.; Allen, D. *Renew. Sust. Energ. Rev.* **2015,** *52,* 418–429.

[14] Dahms, H.-U.; Ying, X.; Pfeiffer, C. *Biofouling* **2006,** *22,* 317–327.

[15] Armbrust, E. V. *Nature* **2009,** *459,* 185–192.

[16] Brzezinski, M. A.; Villareal, T. A.; Lipschultz, F. *Mar. Ecol. Prog. Ser.* **1998,** *167,* 89–104.

[17] Prihoda, J.; Tanaka, A.; Wilson de Paula, B. M.; Tirichine, J. F. A. L.; Bowler, C. *J. Exp. Bot.* **2012,** *63,* 1543–1557.

[18] Kuczynska, P.; Jemiola-Rzeminska, M.; Strzalka, K. *Mar. Drugs* **2015,** *13,* 5847–5881.

[19] Sarthoua, G.; Timmermans, K. R.; Blaina, S.; Treguer, P. *J. Sea Res.* **2005,** *53,* 25–42.

[20] Bahulikar, R. A.; Kroth, P. G. *Eur. J. Phycol.* **2007,** *42,* 199–208.

[21] Hoagland, K. D.; Rosowski, J. R.; Gretz, M. R.; Roemer, S. C. *J. Phycol.* **1993,** *29,* 537–566.

[22] Molino, P. J.; Wetherbee, R. *Biofouling* **2008,** *24,* 365–379.

[23] Domozych, D. S.; Ciancia, M.; Fangel, J. U.; Mikkelsen, M. D.; Ulvskov, P.; Willats, W. G. T. *Geomicrobiol. J.* **2015,** *32,* 275–290.

[24] Gustavs, L.; Görs, M.; ; Karsten, U. *J. Phycol.* **2011,** *47,* 533–537.

[25] Brinkmann, N.; Hodač, L.; Mohr, K. I.; Hodačová, A.; Jahn, R.; Ramm, J.; Hallmann, C.; Arp, G.; Friedl, T. *Geomicrobiol. J.* **2015,** *32,* 255–274.

[26] Hodaè, L.; Brinkmann, N.; Mohr, K. I.; Arp, G.; Hallmann, C.; Ramm, J.; Spitzer, K.; Friedl, T. *Geomicrobiol. J.* **2015,** *32,* 275–290.

[27] Al-Gheilani, A.; Rowe, W.; Li, Y.; Wong, K. L. *Energy Procedia* **2017,** *110,* 95–100.

[28] Shit, S. C.; Shah, P. *Natl. Acad. Sci. Lett.* **2013,** *36,* 355–365.

[29] Hillborg, H.; Gedde, U. W. *IEEE Trans. Diel. Elect. Insul.* **1999,** *6,* 703–717.

[30] Gustavsson, T.; Gubanski, S.; Hillborg, H.; Karlsson, S.; Gedde, U. *IEEE Trans. Dielectr. Electr. Insul.* **2001,** *8,* 1029–1039.

[31] Bruce, G. P.; Rowland, S. M.; Krivda, A. *IEEE Trans. Dielectr. Electr. Insul.* **2010,** *17,* 521–532.

[32] Amer, M.; Laninga, J.; McDermid, W.; Swatek, D. R.; Kordi, B. *IEEE Trans. Diel. Elect. Insul.* **2018,** *25,* 2452–2460.

[33] Arshad,; Nekahi, A.; McMeekin, S. G.; Farzaneh, M. *Electr. Eng.* **2017,** *99,* 1053–1063.

[34] Zhu, Y.; Haji, K.; Otsubo, M. *IEEE T PLASMA SCI* **2006,** *34,* 1094–1098.

[35] Reddy, B. S.; D, S. P. *IEEE Trans Dielectr Electr Insul* **2016,** *23,* 359–367.

[36] Schirrer, R.; Thepin, P.; Torres, G. *J. Mater. Sci.* **1992,** *27,* 3424–3434.

[37] Fernando, M. A. R. M.; Gubanski, S. M. *IEEE Trans Dielectr Electr Insul* **2010,** *17,* 326–333.

[38] Kim, S.-H.; Cherney, E. A.; Hackam, R. *IEEE Trans. Electr. Insul.* **1992,** *27,* 610–622.

[39] Allen, B.; Bleszynski, M.; Kumosa, M.; Willis, E. *IEEE Trans Dielectr Electr Insul* **2015,** *22,* 2978–2986.

[40] Bleszynski, M.; Kumosa, M. *IEEE Trans Dielectr Electr Insul* **2016,** *23,* 2822–2829.

[41] Ghosh, D.; Bhandari, S.; Chaki, T. K.; Khastgir, D. *RSC Adv.* **2015,** *5,* 57608–57618.

[42] Ghosh, D.; Khastgir, D. *ACS Omega* **2018,** *3,* 11317–11330.

[43] Huh, C.-S.; Youn, B.-H.; Lee, S.-Y. *Proceedings of the 6th International Conference on Properties and Applications of Dielectric Materials (Cat. No.00CH36347)* **2000,** *1,* 367–370.

[44] Amin, M.; Akbar, M.; Amin, S. *Rev. Adv. Mater. Sci.* **2007,** *16,* 10–26.

[45] Wallströma, S.; Dowling, K.; Karlsson, S. *Polym.* **2002,** *78,* 257–262.

[46] Wallström, S.; Karlsson, S. *Polym. Degrad. Stabil.* **2004,** *85,* 841–846.

[47] Xie, C.; Li, C.; Zhu, W.; Gan, Y. *Int. Conf. Electrical Materials and Power Equipment* **2017,** *1,* 664–666.

[48] Ouyang, X.; Yin, F.; Jia, Z.; Yang, S.; Wang, Y.; Bai, H.; Zhang, X.; Li, Y.; Chen, H. *ELECTR POW SYST RES* **2019,** *167,* 138–149.

[49] Bixler, G. D.; Bhushan, B. *Phil. Trans. R. Soc.* **2012,** *370,* 2381–2417.

[50] Trueba, A.; Otero, F. M.; González, J. A.; Vega, L. M.; García, S. *Biofouling* **2013,** *29,* 1139–1151.

[51] Lichtenberg, J. Y.; Ling, Y.; Kim, S. *Sensors* **2019,** *19,* 2488–2505.

[52] Struzyna, L. A.; Katiyar, K.; Cullen, D. K. *Curr. Opin. Solid State Mater. Sci.* **2014,** *18,* 308–318.

[53] Compain, E.; Poirier, S.; Drevillon, B. *Appl. Opt.* **1999,** *38,* 3490–3502.

[54] Mulansky, S.; Saballus, M.; Friedrichs, J.; Bley, T.; Boschke, E. *Eng. Life Sci.* **2017,** *27,* 833–840.

[55] Yamasaki, H.; Morita, S. *J. Appl. Poly. Sci.* **2011,** *119,* 871–881.

[56] Puech, P.-H.; Poolec, K.; Knebelc, D.; Muller, D. J. *Ultramicroscopy* **2006,** *106,* 637–644.

[57] Silva-Dias, A.; Miranda, I. M.; Rocha, R.; Monteiro-Soares, M.; Salvador, A.; Rodrigues, A. G.; C., P.-V. *Cytometry Part A* **2012,** *81A,* 265–270.

[58] Lotz, M. M.; Burdsal, C. A.; Erickson, H. P.; McClay, D. R. *J. Cell Biol.* **1989,** *109,* 1795–1805.

[59] Usami, S.; hsu Chen, H.; Zhao, Y.; Chien, S.; Skala, R. *Ann. Biomed. Eng.* **1993,** *21,* 77–83.

[60] Lawrence, M.; Mclntire, L.; Eskin, S. *Blood* **1987,** *70,* 1284–1290.

[61] Cao, J.; Usami, S.; Dong, C. *Ann. Biomed. Eng.* **1997,** *25,* 573–580.

[62] Ozkan, A.; Berberoglu, H. *Biofouling* **2013,** *29,* 469–482.

[63] Ozkan, A.; Berberoglu, H. *Colloids Surf., B* **2013,** *112,* 302–309.

[64] Toschi, F.; Sega, M., Eds.; *Flowing Matter;* Springer: Sham, Switzerland, 2019.

[65] Wiklund, K.; Zhang, H.; Stangner, T.; Singh, B.; Bullitt, E.; Andersson, M. *Microbiol.* **2018,** *164,* 483–494.

[66] Brenner, H. *J. Fluid Mech.* **1962,** *12,* 35–48.

[67] Chang, I.-D. *Z. Angew. Math. Phys.* **1961,** *12,* 6–14.

[68] Richou, A. B.; Ambari, A.; Lebey, M.; Naciri, J. *Chem. Eng. Sci.* **2005,** *60,* 2535–2543.

[69] Hou, L.; Park, H.; Okada, S.; Ohama, T. *PROTOPLASMA* **2013,** *251,* 191–199.

[70] Lee, J.-C.; Baek, K.; Kim, H.-W. *J. Clean. Prod.* **2018,** *180,* 244–251.

[71] Cohen, Z. *Chemicals from Microalgae;* Taylor & Francis: London, 1999.

[72] Andersen, R. A. *Algal Culturing Techniques;* Elsevier: Burlington, 2005.

[73] andTaylor L. Weiss, H. S. K.; Thapa, H. R.; Devarenne, T. P.; Han, A. *LAB CHIP* **2014,** *14,* 1415–1425.

[74] Sun, V.; Jarisz, T. A.; Hore, D. K. *Langmuir* **2020,** *36,* 2120–2128.

[75] Schneider, C. A.; Rasband, W. S.; Eliceiri, K. W. *Nat. Methods* **2012,** *9,* 671–675.

[76] Debonand, A. P.; Wootton, R. C. R.; ; Elvira, K. S. *Biomicrofluidics* **2015,** *9,* 024119.

[77] Busscher, H. J.; van der Mei, H. C. *Clin. Microbiol. Rev.* **2006,** *19,* 127–141.

[78] Bos, R.; C., H.; van der Mei,; Busscher, H. J. *FEMS Microbiol. Rev.* **1999,** *23,* 179–230.

[79] Chen, I.-J.; Lindner, E. *Langmuir* **2007,** *23,* 3118–3122.

[80] Bausch, G. G.; Stasser, J. L.; Tonge, J. S.; Owen, M. J. *Plasma Polym.* **1998,** *3,* 23–34.

[81] Maji, D.; Lahirib, S. K.; Das, S. *Surf. Interface Anal.* **2012,** *44,* 62–69.

[82] Wes, J. K. *J. Biomed. Mater. Res.* **1997,** *35,* 505–511.

[83] McCabe, R. M.; Hickey, B. M.; Kudela, R. M.; Lefebvre, K. A.; Adams, N. G.; Bill, B. D.; Gulland, F. M. D.; Thomson, R. E.; Cochlan, W. P.; Trainer, V. L. *Geophys. Res. Lett.* **2016,** *43,* 366-10–376.

[84] Whittaker, K. A.; Rignanese, D. R.; Olson, R. J.; Rynearson, T. A. *BMC Evol. Biol.* **2012,** *12,* 209.

[85] Hasle, G. R. *Deep Sea Res. Oceanogr. Abstr.* **1976,** *23,* 319–338.

[86] Schone, H. *Mar. Biol.* **1972,** *13*, 284–291.

[87] Schone, H. *Mar. Biol.* **1974,** *27*, 287–298.

[88] Leblanc, K. *et al. Earth Syst. Sci. Data* **2012,** *4,* 149–165.

[89] Berges, J.; Franklin, D.; Harrison, P. *J. Physology* **2001,** *37,* 1138–1145.

[90] Guillard, R. R. L.; Hargraves, P. E. *Phycologia* **1993,** *32,* 234–236.

[91] Finlay, J. A.; Schultz, M. P.; Cone, G.; Callow, M. E.; Callow, J. A. *Biofouling* **2013,** *29,* 401–411.

[92] Holland, R.; Dugdale, T. M.; Wetherbee, R.; Brennan, A. B.; Finlay, J. A.; Callow, J. A.; Callow, M. E. *Biofouling* **2007,** *20,* 323–329.

[93] Lee, J. N.; Park, C.; Whitesides, G. M. *Anal. Chem.* **2003,** *75,* 6544–6554.

[94] Koh, K.-S.; Chin, J.; Chia, J.; Chiang, C.-L. *Micromachines* **2012,** *3,* 427–441.

[95] Zheng, B.; Roach, L. S.; Ismagilov, R. F. *J. Am. Chem. Soc.* **2003,** *125,* 11170–11171.

[96] Alles, M.; Rosenhahn, R. *Biofouling* **2015,** *31,* 469–480.